# Roles of SHANK2 in the establishment of stereociliary bundle architecture and auditory function

**Choi, Han Seul**

**Department of Medical Science**

**Graduate School**

**Yonsei University**

# Roles of SHANK2 in the establishment of stereociliary bundle architecture and auditory function

**Advisor Bok, Jinwoong**

**A Dissertation Submitted**
**to the Department of Medical Science**
**and the Committee on Graduate School**
**of Yonsei University in Partial Fulfillment of the**
**Requirements for the Degree of**
**Doctor of Philosophy in Medical Science**

**Choi, Han Seul**

**June 2025**

**Roles of SHANK2 in the establishment of stereociliary bundle architecture and auditory function**

**This Certifies that the Dissertation of Choi, Han Seul is Approved**

| | |
|---|---|
| **Committee Chair** | Lee, Min Goo |
| **Committee Member** | Bok, Jinwoong |
| **Committee Member** | Gee, Heon Yung |
| **Committee Member** | Moon, Seok Jun |
| **Committee Member** | Lee, Ji Eun |

**Department of Medical Science**
**Graduate School**
**Yonsei University**
**June 2025**

# ACKNOWLEDGEMENTS

It is with immense gratitude that I acknowledge the support and encouragement I have received throughout my Ph.D. course.

First, I would like to express my deepest thanks to my thesis supervisor, Prof. Jinwoong Bok, whose guidance, patience, and unwavering support have been invaluable. His mentorship was instrumental in my research as well as my personal growth.

I am also grateful to my thesis committee members, Prof. Min Goo Lee, Prof. Heon Yung Gee, Prof. Seok Jun Moon, and Prof. Ji Eun Lee. Their insightful comments, constructive feedback, and guidance have greatly contributed to the quality and depth of my thesis.

Also, I would like to express my gratitude to my lab members who have been a part of this journey. I am thankful for the collaborative spirit and the opportunity to work with such supportive colleagues. Their willingness to share ideas and support has greatly contributed to my personal and professional growth.

To my family, I extend my heartfelt thanks. My parents have been my pillars of strength, providing endless support and encouragement throughout this journey. I am deeply thankful to my husband for his unwavering belief in me, his patience, and his constant support. Special thanks to my grandmother for her love and encouragement, and to my in-laws for their support and understanding during these demanding years.

I am grateful to everyone who has played a role in helping me reach this significant milestone. Thank you all for being a part of this journey with me.

Han Seul Choi
June 2025

많은 분들의 도움과 격려가 있었기에 제가 긴 박사과정을 무사히 마칠 수 있었다고 생각합니다. 먼저, 저의 지도교수이신 복진웅 교수님께 진심으로 감사드립니다. 교수님의 끊임없는 지도와 인내, 그리고 무한한 지원 덕분에 연구자로서 많은 것을 배우고 성장할 수 있었습니다.

또한, 논문 심사위원이신 이민구 교수님, 지헌영 교수님, 문석준 교수님, 이지은 교수님께도 감사의 말씀을 전합니다. 교수님들의 날카로운 조언들이 있었기에 제 논문의 질이 한층 높아질 수 있었습니다.

학위과정을 거치며 만났던 모든 연구실 식구들에게도 감사의 말씀을 전합니다. 항상 서로 도와주고, 연구에 대해 편안하게 의견을 나누며 함께 발전할 수 있는 동료들을 만난 덕분에 연구뿐만 아니라 저 자신도 크게 성장할 수 있었습니다.

가족들에게도 깊은 감사의 마음을 전합니다. 긴 시간 언제나 저를 믿고 지지해주신 부모님께 무한한 감사의 말씀을 드리며, 가까이에서 저를 응원해준 남편에게도 깊은 사랑과 감사의 마음을 전합니다. 사랑하는 외할머니께도 따뜻한 격려와 사랑에 감사드립니다. 변함없이 이해하고 지원해주신 시댁 식구들께도 감사드립니다.

일일이 나열하지는 못했지만 제 학위과정을 함께해주신 모든 분들께 진심으로 감사드립니다. 학위과정 중 만난 모든 분들 덕분에 이 중요한 시기를 잘 이겨내고 연구를 마무리할 수 있었습니다. 감사합니다.

2025 년 6 월 최한슬 올림

# TABLE OF CONTENTS

# LIST OF FIGURES

# LIST OF TABLES

## ABSTRACT

### Roles of SHANK2 in the establishment of stereociliary bundle architecture and auditory function

Effective sound transduction in mammals depends on the precise organization of the hair cell stereociliary bundle. Each bundle comprises around 100 actin-filled stereocilia arranged in a three-row staircase pattern. In inner hair cells, this arrangement forms a broad U-shape, whereas in outer hair cells, it takes on a characteristic V-shape—an architectural feature unique to the mammalian cochlea. The vertices of these bundles are uniformly oriented laterally along the cochlear duct. Developmental transition from evenly distributed microvilli to this unique bundle architecture is guided by the lateral movement of the microtubule-based kinocilium, which is controlled by proteins on the lateral surface, such as Gαi and GPSM2. While the role of these lateral proteins is well established, the mechanisms on the medial side remain unclear. Our study identified SHANK2, a protein associated with synaptic function and autism spectrum disorders, as a critical player in establishing the U- or V-shaped bundle architecture on the medial surface. SHANK2 localization is regulated by the small GTPase RAP1, independently of lateral proteins such as Gαi and GPSM2 or medial proteins such as aPKCζ and PARD6B. In *Shank2*-deficient mice, hair cells lose their typical U- or V-shaped bundle architecture, exhibiting a fragmented or wavy appearance without affecting other critical features such as kinocilium position, staircase pattern, and essential stereociliary links. Despite widespread bundle defects across the tonotopic axis, auditory function is specifically impaired at high frequencies, primarily due to compromised OHC amplifier function. Longitudinal studies further suggest that this unique architecture is essential for the long-term maintenance of bundle integrity and auditory function.

---

Key words : hair cell, stereocilia, cochlea, hearing loss, autism spectrum disorder

# 1. Introduction

The cochlea in mammals contains specialized auditory hair cells (HCs) that are finely tuned to transform sound vibrations (mechanical stimuli) into electrical signals. Each hair cell has a stereociliary bundle made up of around 100 actin-filled stereocilia, arranged in a three-row staircase pattern. Inner hair cells (IHCs), which mainly send sound information to the brain, have a broad U-shaped stereociliary bundle. On the other hand, outer hair cells (OHCs), which amplify and refine sound signals to improve cochlear sensitivity and selectivity, feature a V-shaped stereociliary bundle [1,2]. In both types of hair cells, a kinocilium, which is a microtubule-based primary cilium of hair cells, is positioned at the apex of the U- or V-shaped arrangement and oriented laterally along the cochlear duct.

In the early stages of development, immature hair cells have a symmetrical apical surface arrangement with the kinocilium positioned centrally among evenly distributed microvilli (Fig. 3H) [3]. As development prceeds, the kinocilium shifts laterally, resulting in a microvilli-free area, bare zone, on the lateral side [4,5]. The remaining microvilli on the medial surface then arrange into a U- or V-shaped bundle, forming a three-row staircase pattern (Fig. 3H) [3]. This shift from a symmetrical to an asymmetrical architecture in each hair cell, along with the uniform alignment of these bundles throughout the cochlea, is critical for the hair cells to generate coordinated and directionally precise responses to sound waves [6,7].

The uniform orientation of hair cells is controlled by the planar cell polarity (PCP) signaling pathway. Core PCP components, including Van Gogh-like 2 (VANGL2), Scribble 1 (SCRB1), Dishevelled (DVL1 and DVL2), and Frizzled (FZ3 and FZ6), play a crucial role in establishing the organized orientation of hair cells [7-10]. Mutations in these core PCP proteins disrupt the uniform alignment of hair cells, although each cell still has its U- or V-shaped hair bundle arranged in a three-row staircase pattern, albeit oriented randomly. This indicates that the mechanisms responsible for establishing the asymmetric hair bundle structure are different from those regulating the uniform orientation of hair cells.

The formation of asymmetry in each hair cell is regulated by proteins such as G protein alpha i subunit (Gαi) and G protein signaling modulator 2 (GPSM2), which are localized on the lateral surface of developing hair cells [4,5]. These proteins guide the lateral movement of the kinocilium by

regulating the pulling forces exerted on the microtubule cytoskeleton. Mutations in these proteins impair the organization of the U- or V-shaped stereociliary bundles [4,5]. Furthermore, Dishevelled-associating protein with a high frequency of leucine residues (DAPLE) and Partitioning defective 3 (PARD3) link PCP components to the microtubule network, and malfunction of these proteins affects both the orientation of hair cells and the architecture of individual hair bundles, highlighting the complexity of these processes [11-13].

Despite notable advancements, two key questions remain unresolved: what are the mechanisms that shape the U- or V-shaped bundle architecture on the medial surface of hair cells, and what is the specific role of this unique architecture in auditory function? Existing mouse models with disrupted U- or V-shaped bundles, such as Gαi, GPSM2, DAPLE, and PARD3 mutant mice, also exhibit defects with hair cell orientation or the three-row staircase pattern [4,11-15], leading to hearing loss that is not directly related to the bundle architecture and complicates the assessment of its *in vivo*.

In this study, we identify SHANK2 as a medial surface protein crucial for the establishment of the U- or V-shaped hair bundle architecture without altering other critical structures such as kinocilium, staircase arrangement, and essential stereociliary links. The small GTPase RAP1 is required for the recruitment and maintenance of SHANK2 at the medial apical surface of auditory HCs. Our findings demonstrate that this distinct architecture is vital for high-frequency hearing and for the long-term preservation of bundle integrity and auditory function.

# 2. Materials and methods

## 2.1. Mice

*Shank2*$^{-/-}$ mice [16] were maintained in a C57BL/6N background. HC-specific and SGN (spiral ganglion neuron)-specific *Shank2* conditional knockout (cKO) mice were generated by crossing *Shank2*$^{lox/lox}$ mice [17] with *Gfi1*$^{Cre/+}$ mice [18] and *Bhlhe22*$^{Cre/+}$ mice [19], respectively. Both cKO mice were maintained in a C57BL/6J background. *Gpsm2*$^{-/-}$ (*Gpsm2*$^{tm1a}$) mice [5] were purchased from the European Mouse Mutant Archive (EMMA) and maintained in a C57BL/6N background. Otic-specific and HC-specific *Rap1a/b* double cKO (dcKO) mice were generated by crossing *Rap1a/b* double floxed mice (*Rap1a*$^{tm1Morz}$; *Rap1b*$^{tm1Morz}$, JAX; stock #021066) [20] with *Slc26a9*$^{Cre/+}$ (*Slc26a9*$^{P2ACre}$) [21] and *Gfi1*$^{Cre/+}$ mice, respectively. *Rap1a/b* dcKO mice were maintained in a C57BL/6J background. All animals were handled in accordance with the guidelines for the Institutional Animal Care and Use Committee at Yonsei University College of Medicine.

## 2.2. *In situ* hybridization

Embryos and mice were fixed overnight in 4% paraformaldehyde (PFA), dehydrated using 30% DEPC treated sucrose and embedded in Tissue-tek optimal cutting temperature (O.C.T.) compound (Sakura Finetek, Torrance, California, USA). Frozen sections were performed at 12 μm thickness using the HM525 cryostat (Thermo Fisher Scientific, Waltham, Massachusetts, USA). *In situ* hybridization was performed as previously described [22,23] using antisense RNA probes for *Shank2* (+3660 – +4965, NM_001081370.2), *Atoh1*, *Smpx* and *Nefl*. Images were taken using a DM2500 optical microscope (Leica Microsystems, Wetzlar, Germany).

## 2.3. Gene expression analysis using public RNA-sequencing datasets

To analyse the expression pattern of SHANK family genes (*Shank1*, *Shank2*, and *Shank3*) in the embryonic and mature cochlea, previously published RNA-sequencing datasets were utilized: a single-cell RNA-sequencing dataset from the developing cochlea (E14.5 to P3) [24], a single-cell RNA-sequencing dataset from SGNs at P25- 27 [25], and a bulk RNA-sequencing dataset from isolated IHCs, OHCs, Deiters' cells, and pillar cells at P28-35 [26,27]. The H5AD files for the two single-cell

RNA-sequencing datasets were acquired from gEAR portal (https://umgear.org/) [28]. For the bulk RNA-sequencing dataset, we utilized the RPKM values for all genes and samples as provided in the original publications. As the files were pre-quality-controlled, preprocessed, and annotated by the original authors, we performed minimal additional processing. All analyses and visualization were conducted using R (version 4.4.1).

## 2.4. Immunofluorescence

Mice inner ears were fixed with 4% PFA or 10% trichloroacetic acid (TCA) for 30 minutes, then washed three times with 0.02% sodium azide containing phosphate-buffered saline (PBS). Cochlear and vestibular epithelia were micro-dissected in PBS using forceps, permeabilized with 5% Triton X-100, and blocked with 5% normal serum and 3% BSA containing 0.02% sodium azide. Tissues were incubated with primary antibodies overnight at 4℃. After washing with PBS 8 times, tissues were incubated with secondary antibodies (1:250, #A-11001, #A-11008, #A32802, #A32788, Invitrogen, Waltham, Massachusetts, USA, and #ab150185, Abcam, Cambridge, UK) with Phalloidin (1:200, #A12380) or peanut agglutinin (PNA) (1:100, #L32458, Invitrogen, Waltham, Massachusetts, USA) for 2 hours at room temperature. Samples were washed 8 times and mounted with ProLong Gold Antifade Mountant (P36930, Invitrogen, Waltham, Massachusetts, USA). Images were taken by a LSM980 confocal microscope (Carl Zeiss, Oberkochen, Germany). The primary antibodies used in this study are: anti-SHANK2 (1:200, #162 204 and #162 202, Synaptic Systems, Göttingen, Germany), anti-Gαi (1:600, #G4040) and anti-γ-Tubulin (1:100, T3195, Sigma-Aldrich, St. Louis, Missouri, USA), anti-GPSM2 (1:200, #11608-2-AP, Proteintech, Rosemont, Illinois, USA), anti-aPKCζ (1:100, #sc-17781) anti-PARD6B (1:100, #sc-166405) and anti-LMO7 (1:200, #sc-376807, Santa Cruz, Dallas, Texas, USA), anti-β-Spectrin (1:500, #612562, BD Biosciences, Franklin Lakes, New Jersey, USA), anti-ZO-1 (1:200, #61-7300 and #33-9100, Invitrogen, Waltham, Massachusetts, USA), and anti-ARL13B (1:500, gifts from H. W. Ko, Yonsei University) [29].

## 2.5. Scanning electron microscopy (SEM)

Mice inner ears were fixed with SEM fixative (2.5% glutaraldehyde and 2% PFA in 0.1 M sodium cacodylate buffer containing 2 mM calcium chloride) at 4℃. Fixed inner ears were

decalcified with 0.2 M EDTA, micro-dissected in wash buffer (0.1 M sodium cacodylate buffer with 2 mM calcium chloride), and dissected cochlea were fixed overnight in 3.5% sucrose containing SEM fixative. Cochlea were washed with wash buffer on ice, post-fixed in 1% osmium tetroxide ($OsO_4$)/ 1% thiocarbohydrazide (TCH)/ 1% $OsO_4$ (OTO protocol). For cochlea obtained from mice less than 2 weeks of age and explant cultures, post-fixation was performed with an OTOTO protocol. Post-fixed cochlea were dehydrated using a graded ethanol series and dried using a critical point dryer. The dried samples were coated with platinum and SEM images were taken by a JSM-IT-500HR (JEOL, Tokyo, Japan).

## 2.6. Auditory brainstem response (ABR)

ABR measurements were performed in a sound-proof chamber using RZ6 digital signal processing hardware and the BioSigRZ software package (Tucker-Davis Technologies, Alachua, Florida, USA). Mice were anesthetized with a mixture of Zoletil (40 mg/kg) and Rompun (10 mg/kg) by intraperitoneal (IP) injection. Subdermal electrodes were placed at the vertex and ventrolateral to the right and left ear of anesthetized mice. Click stimuli (10 μs duration) or tone burst stimuli (5 ms duration) at 4, 6, 12, 18, 24, 20, and 36 kHz were produced using the SigGenRZ software package and an RZ6 digital signal processor, and delivered to the ear canal through a multi-field 1 (MF1) magnetic speaker (Tucker-Davis Technologies). The acoustic stimulus intensity was increased from 5 to 95 dB SPL in 5 dB SPL increments, and the ABR signals were fed into a RA4LI low-impedance Medusa Biological Amplifier System (Tucker-Davis Technologies). The recorded signals were filtered using a 0.5–1 kHz band-pass filter, and the ABR waveforms in response to 256 tone bursts were averaged. The ABR thresholds for each frequency were determined using BioSigRZ software package. ABR wave I amplitudes were analysed at three specific frequencies (6, 18, and 24 kHz) by calculating P1–N1 peak amplitudes (μV) as input/output (I/O) functions with stimulus levels from 30 to 90 dB SPL.

## 2.7. Distortion product otoacoustic emissions (DPOAE)

DPOAE measurements were performed using a combined microphone-speaker system (Tucker-Davis Technologies), primary stimulus tones were generated using RZ6 digital signal processor and the SigGenRZ software package. Stimulus sound was delivered through a custom

probe equipped with MF1 speakers and an ER 10B+ microphone (Etymotic Research, Elk Grove Billage, Illinois, USA) positioned in the ear canal. The $f_1/f_2$ frequency ratio of the primary tones was set at 1.2 with target frequencies of 6, 12, 16, 18, 24, and 30 kHz. The L1 and L2 intensities were set at identical levels and increased from 20 to 80 dB SPL in 5 dB SPL increments. The resultant sounds were received by the ER 10B+ microphone and acquired by the RZ6 digital signal processor. The fast Fourier transform algorithm was used to analyse the average spectra of the tow primaries, the $2f_1$- $f_2$ distortion products, and the noise floors at each primary tone for each intensity. The I/O functions for the DPOAEs were analysed at four specific frequencies (6, 18, 24, and 30 kHz) with stimulus levels from 20 to 80 dB SPL.

## 2.8. Quantitative reverse transcription PCR (RT-qPCR)

Three litters of E16.5 C57BL/6N embryos were harvested in DEPC-treated PBS and each tissue was collected in lysis buffer. RNA was extracted using the RNAqueous™-Micro Total RNA Isolation Kit (AM1931, Invitrogen, Waltham, Massachusetts, USA). cDNA was synthesized using ImProm-II Reverse Transcriptase (A3802, Promega, Madison, Wisconsin, USA) with oligo(dT) primers. qPCR was conducted using the SensiFAST SYBR® Hi-ROX Kit (BIO-92005, Bioline, Cincinnati, Ohio, USA) on a CFX96 Touch Real-Time PCR Detection System (Bio-Rad, Hercules, California, USA). Samples from different litters were processed separately and each sample was run in technical triplicate. The entire experiment was repeated independently three times.

## 2.9. Yeast two-hybrid screening

Yeast two-hybrid screening was conducted by Hybrigenics Services (Évry-Courcouronnes, France). The SHANK2 construct was designed using the coding sequence for *Rattus norvegicus Shank2* (amino acids 1-395, NM_201350.1, pcDNA3.1-rShank2E [30]) and cloned into pB27 as a C-terminal fusion to LexA (N-LexA-Shank2-C). The construct was used as a bait to screen randomly primed cDNA libraries obtained from E16.5 and P2-P6 mice inner ear constructed in pP6 plasmids. The Pridicted Biological Score was automatically computed and ranked from A (high confidence) to D (lower confidence).

## 2.10. Cochlear explant cultures

E14.5 wild-type embryos were harvested and cochlear epithelium was exposed in 5 mM HEPES (Sigma-Aldrich, St. Louis, Missouri, USA) containing HBSS (Gibco). Cochlear epithelium were placed on 6% Matrigel (Corning, Corning, New York, USA)-coated coverslips, and cultured in DMEM supplemented with 10% FBS, 1% N2, and 10 μg/ml ampicillin. After 5–6 hours, 10 μM Rap1 inhibitor (GGTI 298, Cayman Chemical, Ann Arbor, Michigan, USA) or 0.1% DMSO were added. The cochlea were cultured for 6 days in 5% $CO_2$ and constant humidity at 37℃. The last day of culture, cochlea were fixed with 4% PFA or 10% TCA for immunofluorescence, or with SEM fixative (2.5% glutaraldehyde and 2% PFA in 0.1 M sodium cacodylate buffer containing 2 mM calcium chloride) for SEM.

## 2.11. Statistical analysis

All statistical analysis were performed using GraphPad Prism 8.0. All results were expressed as means ± standard deviation. Statistical comparisons were made using two-way analysis of variance (ANOVA) with Bonferroni corrections for multiple comparisons for the ABRs and DPOAEs. For qPCR analysis, one-way ANOVA with Bonferroni corrections was used for statistical comparisons. Statistical significance is indicated as n.s. (non-significant; $P > 0.05$), $*P < 0.05$, $**P < 0.01$, or $***P < 0.001$.

# 3. Result

## 3.1. SHANK2 is expressed in the medial side of apical surface on developing hair cells

### 3.1.1. *Shank2* mRNA is expressed in developing hair cells

We performed *in situ* hybridization to analyze the localization of *Shank2* in the developing mouse cochlea (Fig. 1). At embryonic day (E) 16.5, *Shank2* mRNAs were observed in HCs of the basal cochlear turn as well as in the spiral ganglion neurons (SGNs) (Fig. 1A-D). By postnatal day (P) 1, *Shank2* expression was obviously detected in HCs and SGNs throughout all cochlear turns (Fig. 1E-H). However, by P7, expression in the basal turn decreased (Fig. 1I-L) and was almost undetectable by P14 (Fig. 1M-P).

### 3.1.2. SHANK2 protein is restricted in the medial apical surface of hair cells

To identify the subcellular localization of SHANK2, we performed immunostaining in the developing cochlea. Immunostaining showed that SHANK2 protein was restricted on the medial side of the apical surface of developing hair cells (Fig. 2A-B). At E15.5, SHANK2 expression began on the medial side concurrently with Gαi expression on the lateral side (Fig. 2Cb) [4]. As differentiation continued, the SHANK2 domain expanded toward the center of the cell, while avoiding overlap with the lateral Gαi domain (Fig. 2Ca-Cd). By P1, SHANK2 was distinctly positioned on the medial side, opposite to Gαi and GPSM2, which were localized on the lateral side (Fig. 2A and 3A-B). Proteins typically found on the medial surface, such as atypical PKCζ (aPKCζ) and PARD6B [4,5], had a broader expression domain compared to SHANK2, excluding only the lateral bare zone where Gαi and GPSM2 were expressed (Fig. 3C-D). This specific medial localization of SHANK2 and aPKCζ persisted until P5, with aPKCζ expression being stronger near the base of the stereocilia and SHANK2 remaining prominently expressed near the medial apical surface of the HCs (Fig. 3E and H). Co-immunostaining using the tight junction marker ZO-1 demonstrated that SHANK2 localized reliably to the medial apical surface, without overlapping the ZO-1-marked apical junctional boundary, at both P1 and P5 (Fig. 3F-G). In vestibular HCs, SHANK2 was also localized opposite to Gαi (Fig. 4).

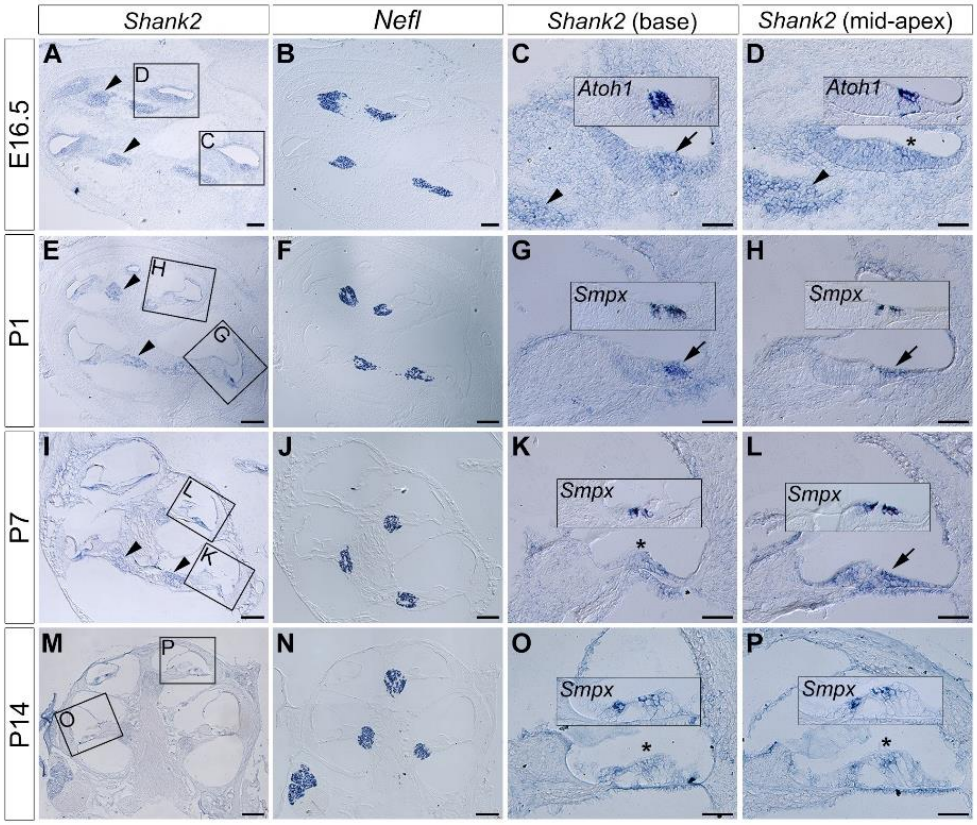


**Fig 1. *Shank2* mRNA is expressed in developing cochlea.** *In situ* hybridization results shows the mRNA expression of *Shank2*, *Nefl* (for SGNs), *Atoh1* and *Smpx* (for HCs). (A-D) At E16.5, *Shank2* expression is evident in SGNs (arrowheads) and HCs in the basal cochlear duct (C, arrow), but not in the mid-apex (D, asterisk). (E-H) By P1, *Shank2* is present in HCs throughout the base (G) and mid-apex (H), as well as in SGNs (E, arrowheads). (I-L) At P7, *Shank2* expression is diminished in HCs in the base (K, asterisk) but still detectable in mid-apex HCs (L, arrow), with weak expression in SGNs (I, arrowsheads). (M-P) At P14, *Shank2* is absent in base HCs (O, asterisk) and barely detected in mid-apex HCs (P, asterisk), with no expression in SGNs (M). Scale bars: A-B, E-F, I-J, M-N, 100 μm; C-D, G-H, K-L, O-P, 50 μm.

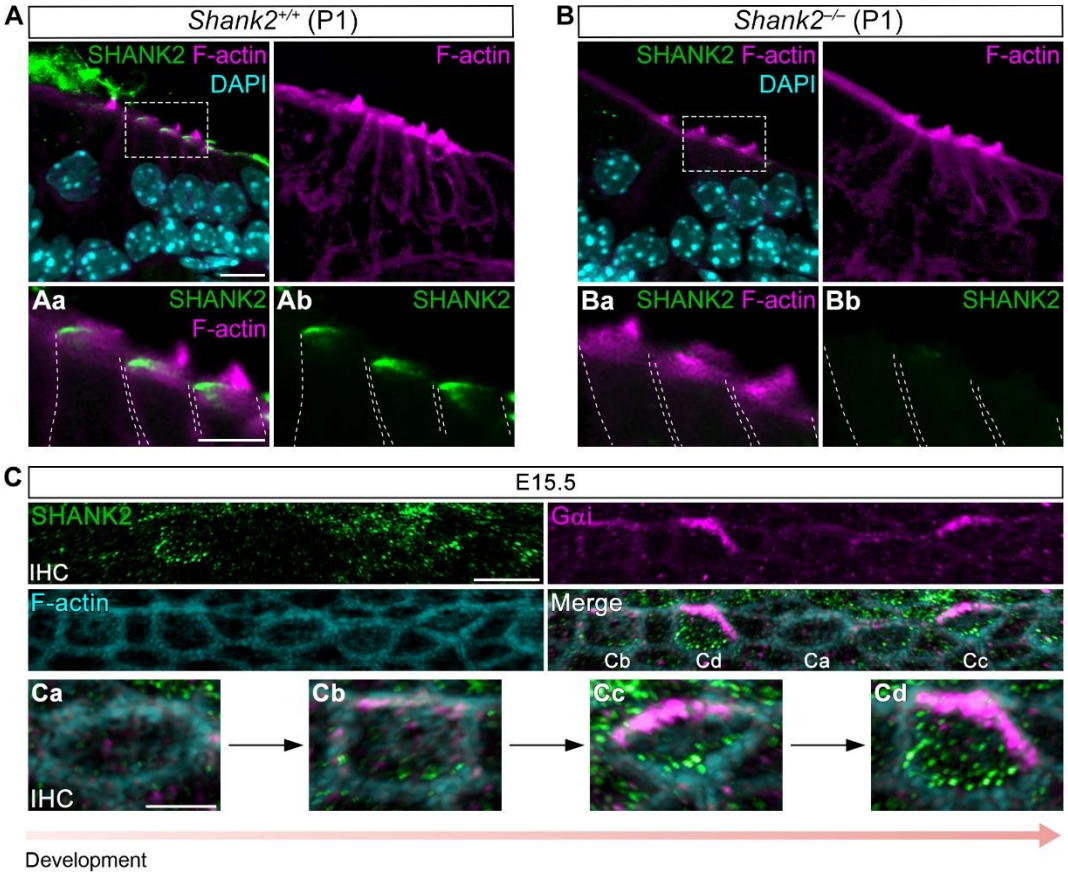


**Fig 2. SHANK2 protein is localized on the medial apical surface in developing hair cells.** (A-B) At P1, cochlear section immunostaining for SHANK2 (green), phalloidin (magenta) and DAPI (cyan). SHANK2 is localized on the medial side of the HC apical surface, but is not found in basolateral membranes or the cell body in *Shank2*$^{+/+}$ mice (A). This SHANK2 signal is completely absent in *Shank2*$^{-/-}$ mice (B). (C) At E15.5, SHANK2 (green) and Gαi (magenta) immunostaining reveals neither protein in immature IHCs (Ca). SHANK2 and Gαi begin to appear from the medial and lateral edges, respectively (Cb). In more mature IHCs, Gαi is confined to the bare zone, while SHANK2 remains on the medial side (Cc-Cd). Scale bars: A-B (upper panels), 10 μm; A-B (lower panels), 5 μm; C, 5 μm; Ca-Cd, 2.5 μm.

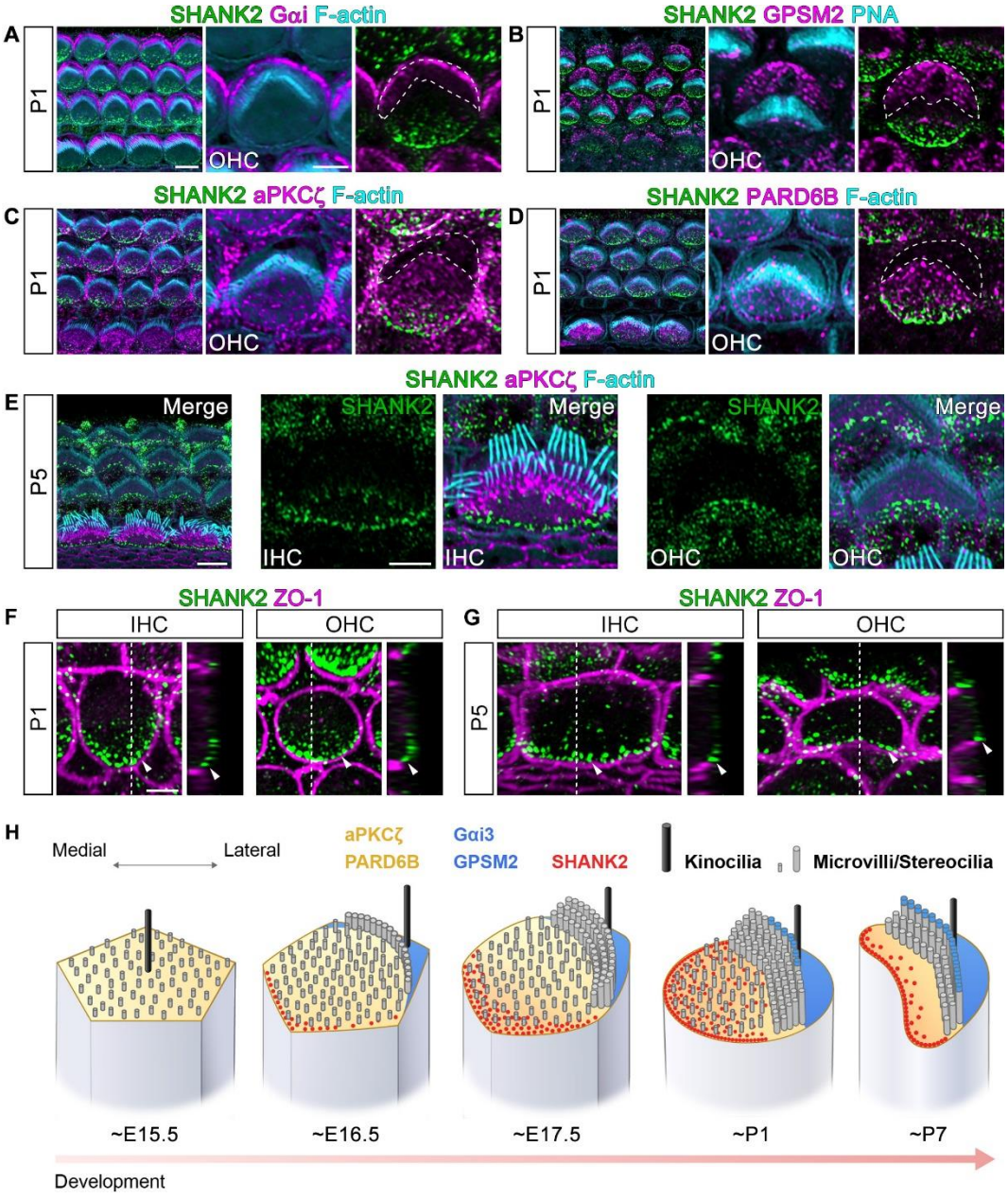


**Fig 3. SHANK2 localization during hair cell differentiation.** (A-D) At P1, SHANK2 is positioned on the medial side of the HC apical surface, while Gαi and GPSM2 are found in the bare zone (A-B, white dashed line). aPKCζ and PARD6B are localized to the medial surface with SHANK2, but

are absent from the bare zone (C-D, white dashed line). (E) By P5, SHANK2 is still present on the medial side, with the strongest signal close to the medial junction and some remaining at the base of the stereocilia. (F-G) In cochlear whole-mounts at P1 (F) and P5 (G), SHANK2 (arrowheads) is confined to the medial apical surface and does not colocalize with ZO-1 at apical junctions. (H) Schematic diagram showing medial and lateral protein localization during HC cytoskeletal development. Scale bars: A-D (left panels), 5 μm; A-D (middle/right panels), 2.5 μm; E (left panel), 5 μm; E (IHC/OHC), 2.5 μm; F-G, 2 μm.

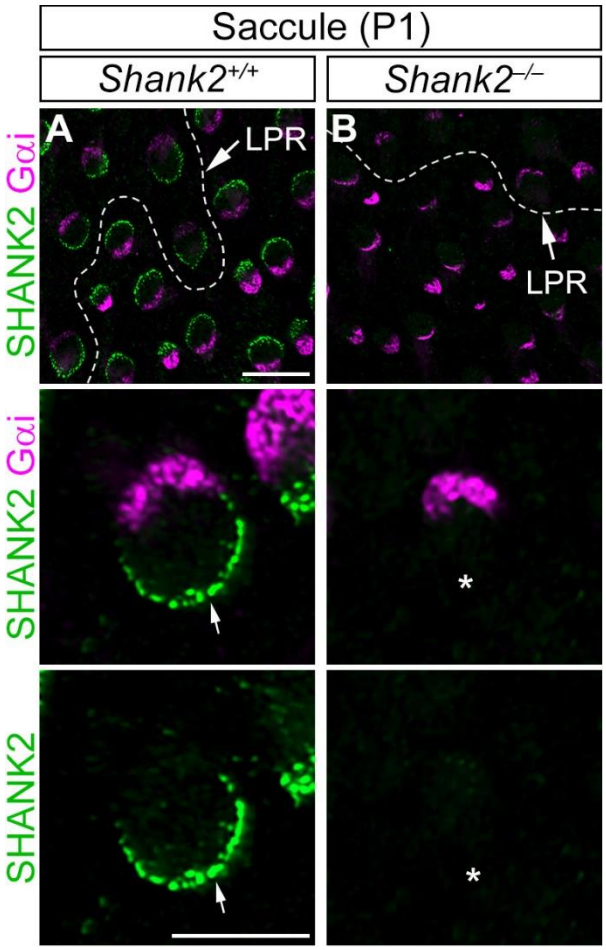


**Fig 4. Localization of SHANK2 in vestibular hair cells.** Whole-mount immunostaining of the saccule at P1. In *Shank2*$^{+/+}$ mice, SHANK2 is positioned opposite to Gαi (A), whereas it is absent in *Shank2*$^{-/-}$ mice (B). LPR: line of polarity reversal. Scale bars: A-B (top panels), 10 μm; middle and bottom panels, 5 μm.

## 3.2. SHANK2 is necessary for the formation of the stereociliary bundle architecture

### 3.2.1. SHANK2 deficiency causes misshapen hair bundle structure without affecting the position of the kinocilium

Given the contrasting expression patterns of SHANK2 and the lateral proteins crucial for asymmetric hair bundle formation, such as Gαi and GPSM2, we hypothesized that SHANK2 plays a role in hair bundle morphogenesis by serving as a medial counterpart to these lateral proteins. In wild-type mice (*Shank2*$^{+/+}$) at E17.5, hair bundles in the basal cochlear turn displayed distinct broad U-shaped patterns in inner hair cells (IHCs) and V-shaped patterns in outer hair cells (OHCs) (Fig. 5A). These bundle arrangement became progressively less pronounced toward the apex, reflecting a base-to-apex gradient in hair cell differentiation (Fig. 5A). In *Shank2*$^{-/-}$ mutants, the characteristic U- or V-shaped bundle structures in IHCs and OHCs were disrupted, appearing wavy or fragmented instead (Fig. 5A). Scanning electron microscopy (SEM) at P0 and P7 confirmed these abnormalities in hair bundle structure for both IHCs and OHCs (Fig. 5B-C). Notably, the hair bundle shapes in vestibular HCs remained largely unaffected in *Shank2*$^{-/-}$ mutants (Fig. 6).

Since mutations in lateral proteins such as Gαi and GPSM2 lead to defects in both hair bundle architecture and kinocilium positioning [4,5], we observed the kinocilium and basal body in *Shank2*$^{-/-}$ mutants (Fig. 7). Remarkably, the position of the basal body (Fig. 7A-B) and kinocilium morphology (Fig. 7C) did not show significant differences between *Shank2*$^{+/-}$ and *Shank2*$^{-/-}$ mice. These findings indicate that SHANK2 is essential for the morphogenesis of stereociliary bundles, while does not play a role in formation and migration of the kinocilium.

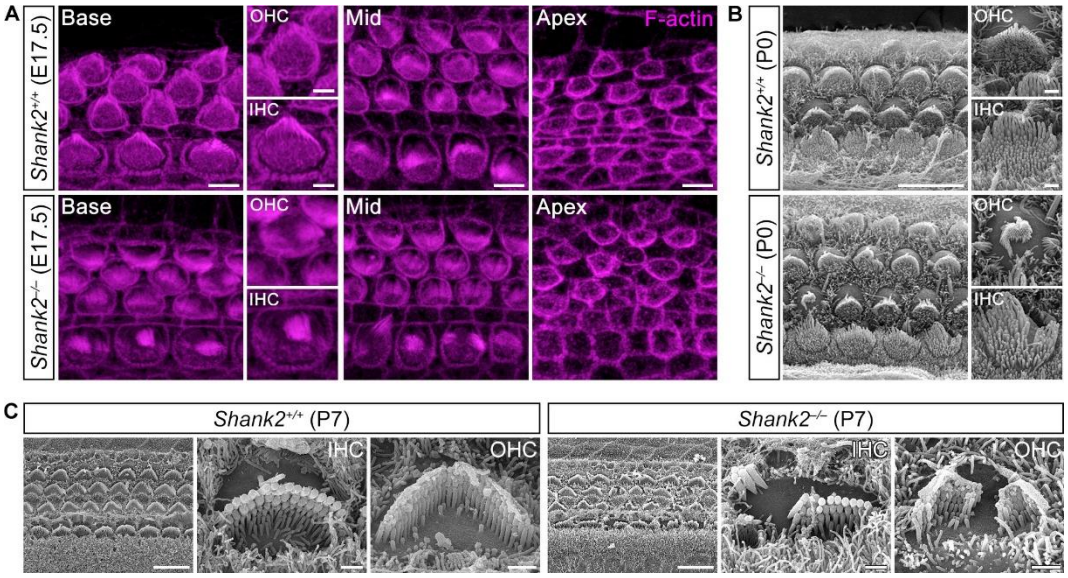


**Fig 5. Hair bundle defects in *Shank2*$^{-/-}$ Cochlea.** (A) Phalloidin staining illustrates hair bundle morphology. At E17.5, wild-type mice exhibit U- or V-shaped stereociliary bundles at the base, with less distinct bundle shapes in the middle and apex of the cochlea. In *Shank2*$^{-/-}$ mice, hair bundles are fragmented or wavy. (B-C) Scanning electron microscope (SEM) images reveal that hair bundle defects persist in both IHCs and OHCs at P0 (B) and P7 (C). Scale bars: A (low magnification), 5 μm; A (IHC/OHC), 2 μm; B (low magnification), 10 μm; B (IHC/OHC), 1 μm; C (low magnification), 10 μm; C (IHC/OHC), 1 μm.

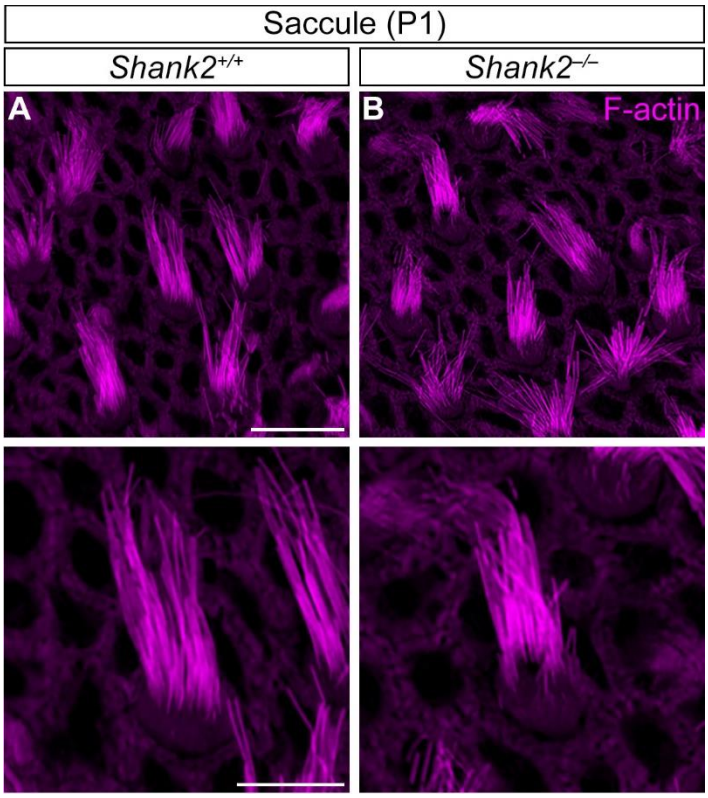


**Fig 6. Morphological changes are not observed in vestibular hair cell of *Shank2* mutant.** The morphology of the stereociliary bundles is comparable between *Shank2*$^{+/+}$ (A) and *Shank2*$^{-/-}$ mice (B). Scale bars: A-B (upper panels), 10 μm; lower panels, 5 μm.

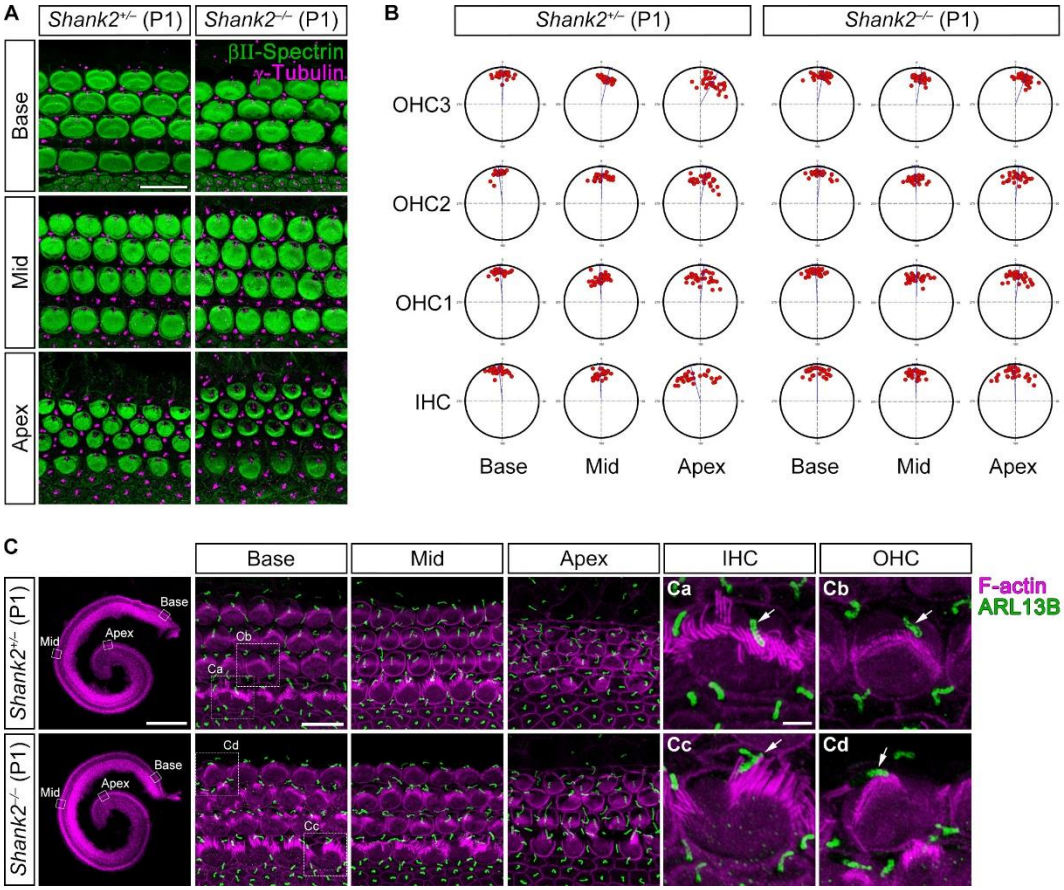


**Fig 7. Hair bundle defects without affecting basal body positioning and kinocilium in *Shank2*$^{-/-}$ Cochlea.** (A) Immunostaining with anti-β-spectrin (green) and anti-γ-Tubulin (magenta) antibodies indicates basal body positioning. (B) Circular histograms plot the position of the basal body. Basal body positioning in *Shank2*$^{-/-}$ cochlea (n = 3) is comparable to that in control cochlea (n = 3). (C) In *Shank2*$^{-/-}$ cochlea, kinocilium (ARL13B, arrows) morphogenesis is unaffected. Scale bars: A, 10 μm; C (whole cochlea), 500 μm; C (low magnification), 10 μm; C (high magnification), 2 μm.

**3.2.2. SHANK2 deficiency results in loss of characteristic U- or V-shaped stereociliary bundle morphology in mature hair cells**

We then assessed the impact of abnormal hair bundle development in mature hair cells in 3-week-old mice. In wild-type mice, IHCs exhibited slightly curved, U-shaped bundles, while OHCs displayed V-shaped hair bundles, both organized in a three-row staircase pattern (Fig. 8A). In *Shank2*$^{-/-}$ mutants, most IHCs and OHCs lost their characteristic U- or V-shaped configurations, showing fragmented or wavy structures along the tonotopic axis of the cochlear duct (Fig. 8B-E). Despite these morphological disruptions, the hair bundles preserved the three-row staircase arrangement (Fig. 9A). Additionally, stereociliary links critical for auditory function, such as tip-links and tectorial membrane (TM) imprints—indicating the connection between OHC stereocilia and the TM [31], remained intact (Fig. 9B-C). These observations suggest that SHANK2 deficiency specifically affects the U- or V-shaped architecture of hair bundles without altering other essential structural features of stereocilia.

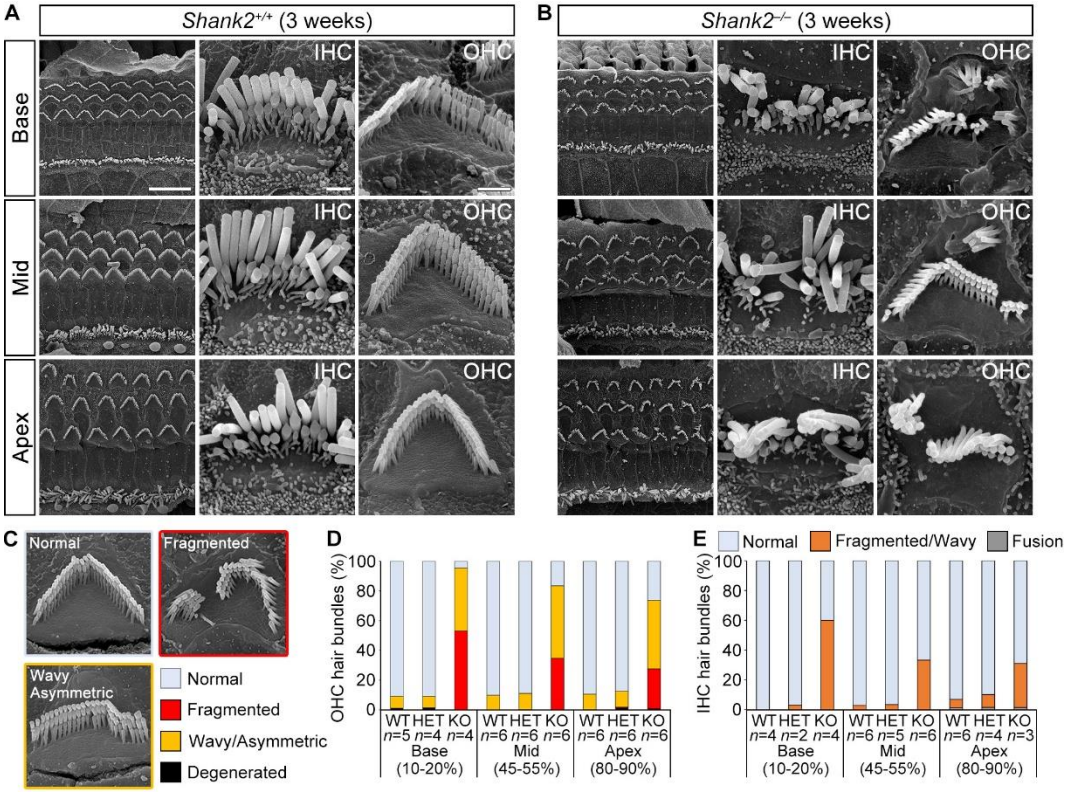


**Fig 8. Loss of U- or V-shaped bundle morphology in mature hair cells in *Shank2*$^{-/-}$ mice.** (A-B) SEM images reveal split or wavy hair bundles throughout the cochlear duct in *Shank2*$^{-/-}$ mice. (C) Examples of OHC bundle defect categories. (D-E) Proportion of OHC (D) and IHC (E) bundle defect in *Shank2*$^{-/-}$ mice. Scale bars: A-B (left panels), 10 μm; A-B (middle/right panels), 1 μm.

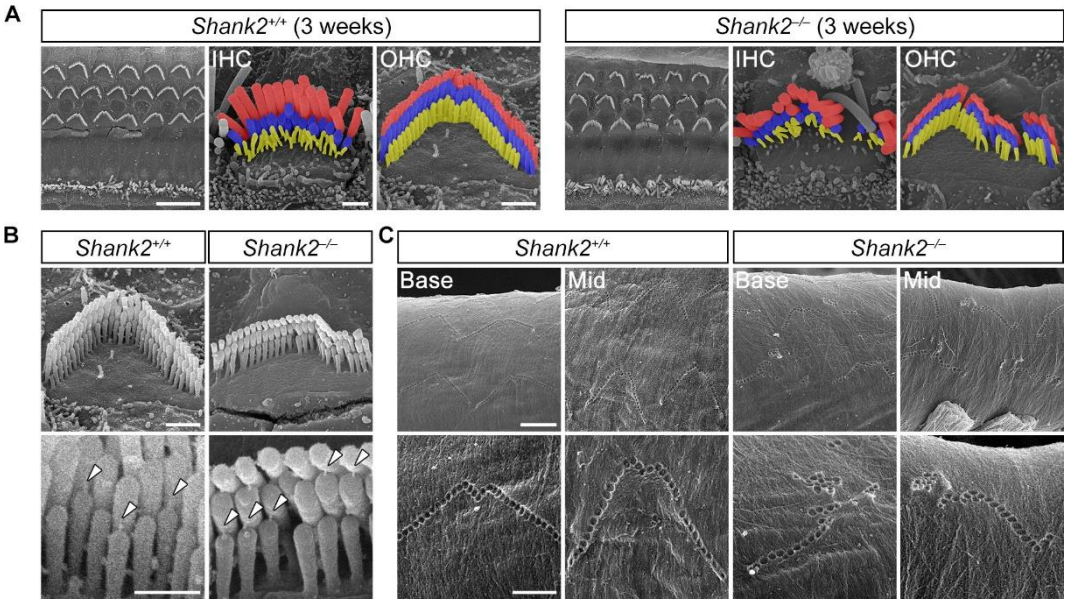


**Fig 9. Unaffected staircase pattern and stereociliary links in 3-week-old *Shank2*$^{-/-}$ mice.** (A) SEM images show that the staircase pattern is preserved, though U- or V-shaped bundle architecture is disrupted in *Shank2*$^{-/-}$ mice. (B-C) Despite the disrupted V-shaped OHC bundle morphology, tip-links (B, arrowheads) and tectorial membrane imprints (C) remain intact in *Shank2*$^{-/-}$ mice. Scale bars: A (low magnification), 10 μm; A (IHC/OHC), 1 μm; B (upper panels), 1 μm; B (lower panels), 0.5 μm; C (upper panels), 2 μm; C (lower panels), 1 μm.

### 3.3. High frequency specific hearing loss in 3-week-old *Shank2* mutants

We evaluated how the loss of the characteristic bundle architecture affects hearing sensitivity at the onset of hearing (3 weeks of age) by measuring ABR thresholds in response to broadband click stimuli and frequency-specific pure tones. Despite the widespread abnormalities in hair bundles along the cochlear duct (Fig. 8), significant shifts in ABR thresholds were only observed at high frequencies, with no notable changes at lower frequencies or in response to click stimuli (Fig. 10A). These data indicate that the U- or V-shaped bundle morphology is specifically important for high-frequency hearing.

ABR threshold shifts can result from various factors. To investigate whether IHCs contribute to the high-frequency-specific threshold shifts, we examined the input/output (I/O) functions of ABR wave I amplitudes, which reflect the synchronized activation of the auditory nerve initiated by neurotransmitter release from IHCs to SGNs [32]. *Shank2*$^{-/-}$ mice exhibited a significant reduction in wave I amplitudes specifically at the high frequency of 30 kHz, while responses at lower frequencies (6, 18, and 24 kHz) remained normal (Fig. 10B). Despite the diminished overall response at 30 kHz, the preserved slope of the input/output function (Fig. 10B) suggests that inner hair cells (IHCs) maintain their capacity to encode sound intensity differences. Additionally, normal interpeak latencies between ABR waves I–IV and I–V indicate that central auditory processing is unaffected in *Shank2*$^{-/-}$ mutants [33] (Fig. 11).

To evaluate OHC function, we measured distortion product otoacoustic emissions (DPOAEs), which indicate the integrity of OHC-mediated cochlear amplification. In *Shank2*$^{-/-}$ mutants, significant shifts in DPOAE thresholds were observed only at high frequencies (Fig. 10C), which consistent with the ABR thresholds shifts (Fig. 10A). Frequency spectrum analysis revealed a marked decrease in $2f_1$-$f_2$ DPOAE amplitude at high frequency (30 kHz), but not at lower frequency (18 kHz) (Fig. 10D-E). The I/O functions of DPOAE amplitudes confirmed no changes at lower frequency (6 kHz), but showed a gradual reduction at higher frequencies (Fig. 10F). These data suggest that the loss of the distinctive hair bundle architecture leads to high-frequency-specific hearing loss primarily due to OHC dysfunction, while IHC function remains relatively unaffected.

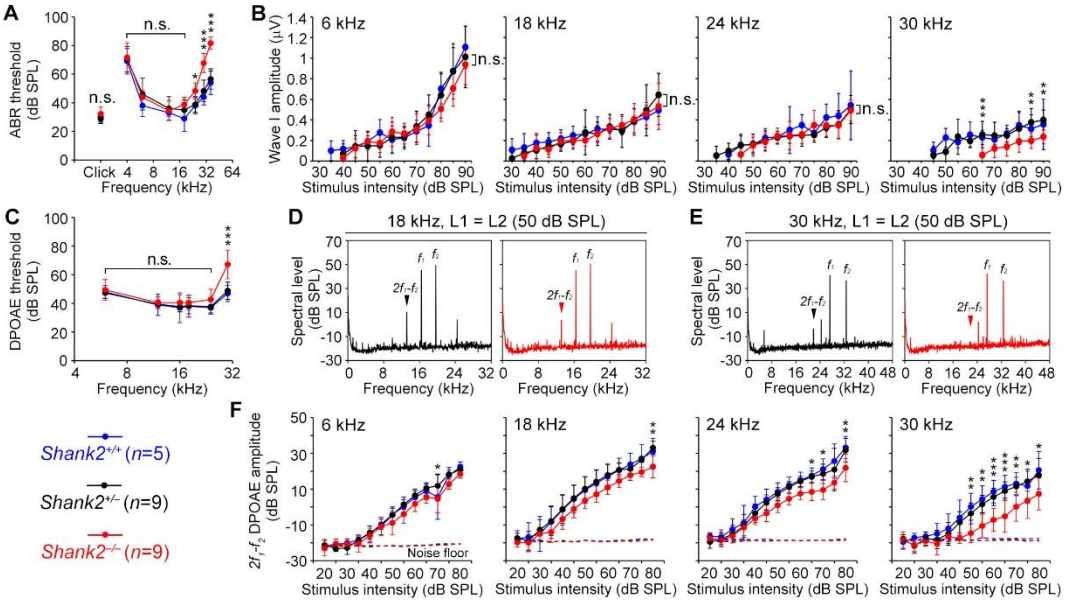


**Fig 10. High frequency hearing loss in 3-week-old *Shank2*$^{-/-}$ mice.** (A-B) ABR measurements for 3-week-old wild-type and *Shank2*$^{-/-}$ mice show significant ABR threshold shifts at high frequencies in *Shank2*$^{-/-}$ mice (A). I/O functions of ABR wave I amplitudes are unchanged except at high intensities at 6 kHz (B). (C-F) DPOAE measurements indicate significant threshold shifts at high frequencies (30 kHz) (C). Frequency spectra reveal reduced $2f_1$-$f_2$ DPOAE amplitudes at 30 kHz (E) but not at 18 kHz (D) in *Shank2*$^{-/-}$ mice. I/O functions of DPOAE amplitudes show progressive reductions at higher frequencies (24 and 30 kHz) (F). Data are presented as means ± standard deviation. Statistical comparisons were performed using two-way ANOVA with Bonferroni correction (n.s., non-significant, *P < 0.05, **P < 0.01, ***P < 0.001).

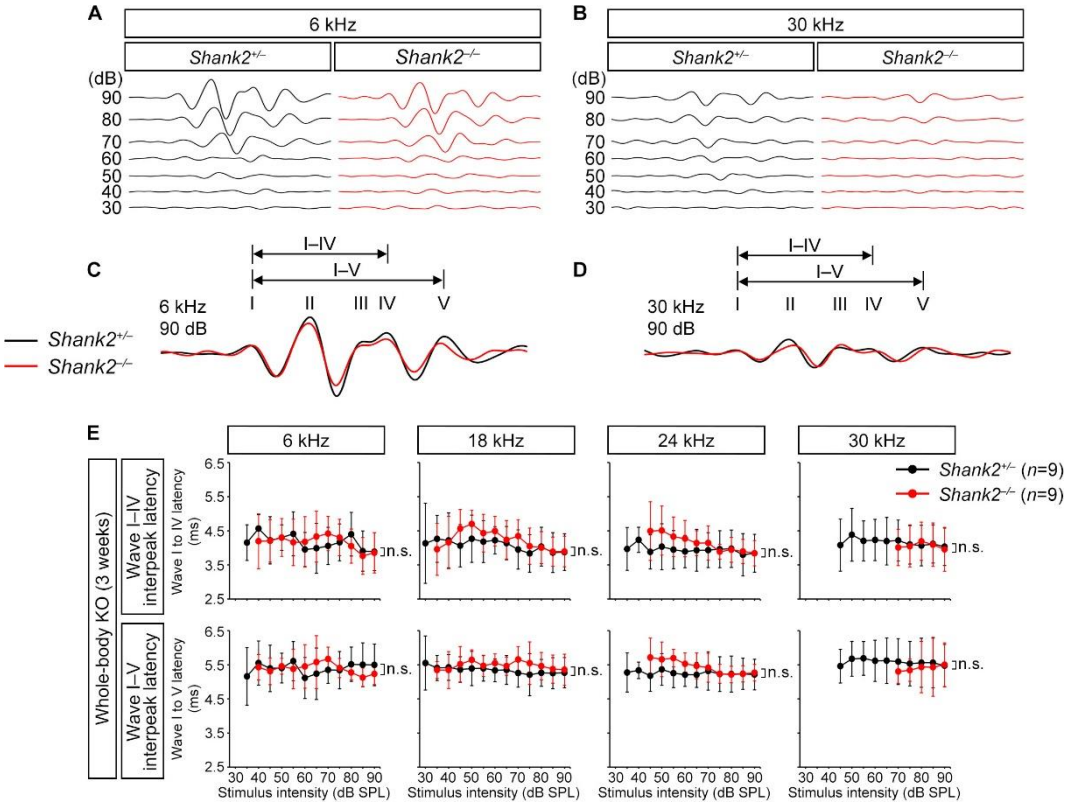


**Fig 11. ABR interpeak latencies are not altered in 3-week-old *Shank2*$^{-/-}$ mice.** (A–B) ABR waveforms recorded at 6 kHz (A) and 30 kHz (B) in *Shank2*$^{-/-}$ mice. (C–D) Representative ABR waveforms at 90 dB for 6 kHz (C) and 30 kHz (D) show no significant differences between *Shank2*$^{+/-}$ and *Shank2*$^{-/-}$ mice. (E–F) Interpeak latencies between waves I–IV and I–V remained within normal range in *Shank2*$^{-/-}$ mice (E). Data are presented as means ± standard deviation. Statistical comparisons were performed using two-way ANOVA with Bonferroni correction (n.s., non-significant).

### 3.4. SHANK2 in hair cells but not in spiral ganglion neurons is critical for hair bundle architecture and hearing function

SHANK2 is crucial for neuronal activities, functioning as a synaptic scaffolding protein in the brain [16,34-36]. However, our analyses suggest that SHANK2 primarily contributes to hearing through its role in HC function—especially OHCs—rather than through auditory nerve activation or central auditory processing (Figs. 10-11). This functional specificity aligns with the distinct cochlear expression patterns of SHANK family genes (*Shank1*, *Shank2*, and *Shank3*) [24-27]. RNA-sequencing data show that *Shank2* is predominantly expressed in embryonic HCs, while *Shank1* is highly expressed in SGNs, with minimal expression of *Shank2* and *Shank3* (Fig. 12A) [24]. In the mature cochlea, all three SHANK genes are downregulated in HCs (Fig. 12B) [26,27], whereas *Shank1* remains robustly expressed across all SGN subtypes (Fig. 12C), consistent with the observed postsynaptic localization of SHANK1—but not SHANK2 or SHANK3—in SGNs [37].

To investigate the specific role of SHANK2 in different cell types for hearing, we generated conditional knockout (cKO) mutants with HC-specific deletion ($Gfi1^{Cre}$; $Shank2^{lox/lox}$) and SGN-specific deletion ($Bhlhe22^{Cre}$; $Shank2^{lox/lox}$). The structural defects in hair bundles seen in systemic *Shank2* mutants ($Shank2^{-/-}$) were also observed in HC-specific mutants (Fig. 13A and C-E) but not in SGN-specific mutants (Fig. 13B) at 3 weeks. Correspondingly, high-frequency ABR and DPOAE threshold elevations were observed in HC-specific mutants (Fig. 14A and D), and the I/O functions of ABR wave I amplitudes were significantly reduced only at high frequency (30 kHz) (Fig. 14B), with normal interpeak latencies of ABR waves I-IV and I-V (Fig. 14C). However, the I/O functions of DPOAE amplitudes revealed a significant reduction at high frequencies in HC-specific mutants (Fig. 14E). Consistent with minimal *Shank2* expression in SGNs (Fig. 12C) [25], SGN-specific *Shank2* mutants showed no significant differences from controls (Fig. 15). These findings highlight that SHANK2 in HCs is essential for establishing the U- or V-shaped hair bundle architecture, which is critical for maintaining high-frequency hearing through its role in OHC amplifier function.

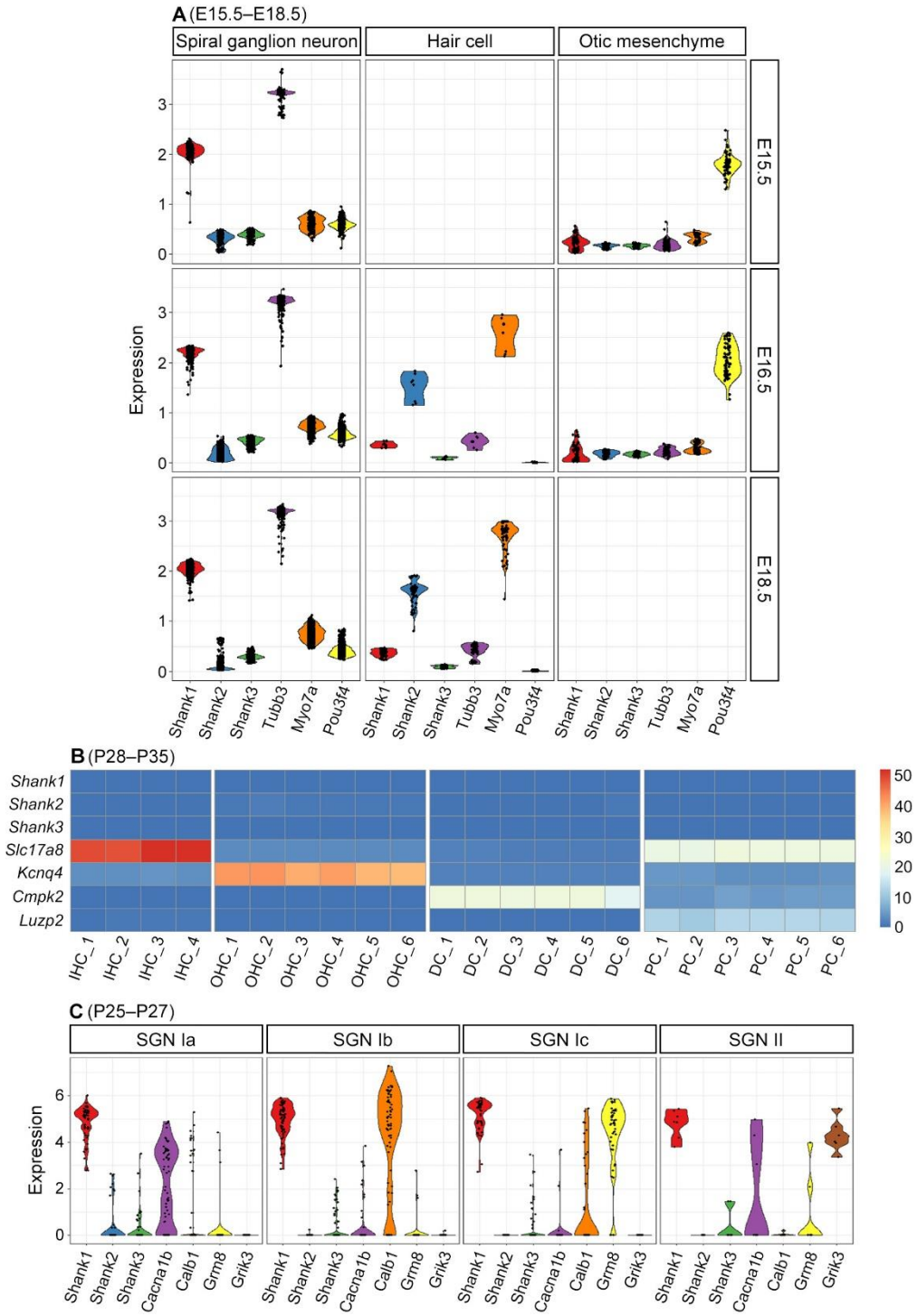

**Fig 12. Expression patterns of SHANK family genes in the cochlea.** Analysis of *Shank1*, *Shank2*, and *Shank3* expression from published RNA-sequencing datasets. (A) Embryonic expression (E15.5, E16.5, and E18.5) in SGNs, HCs, and mesenchymal cells, shown with cell type-specific markers (*Tubb3*, *Myo7a*, and *Pou3f4*) [24]. (B) Postnatal expression (P28-35) in mature cochlear cell types: IHCs, OHCs, Deiters' cells (DCs), and pillar cells (PCs) with corresponding markers (*Slc17a8*, *Kcnq4*, *Cmpk2*, *Luzp2*) [26,27]. (C) Expression in postnatal (P25-27) SGN subtypes (Ia, Ib, and Ic) with subtype-specific markers (*Cacna1b*, *Calb1*, *Grm8*, *Grik3*) [25].

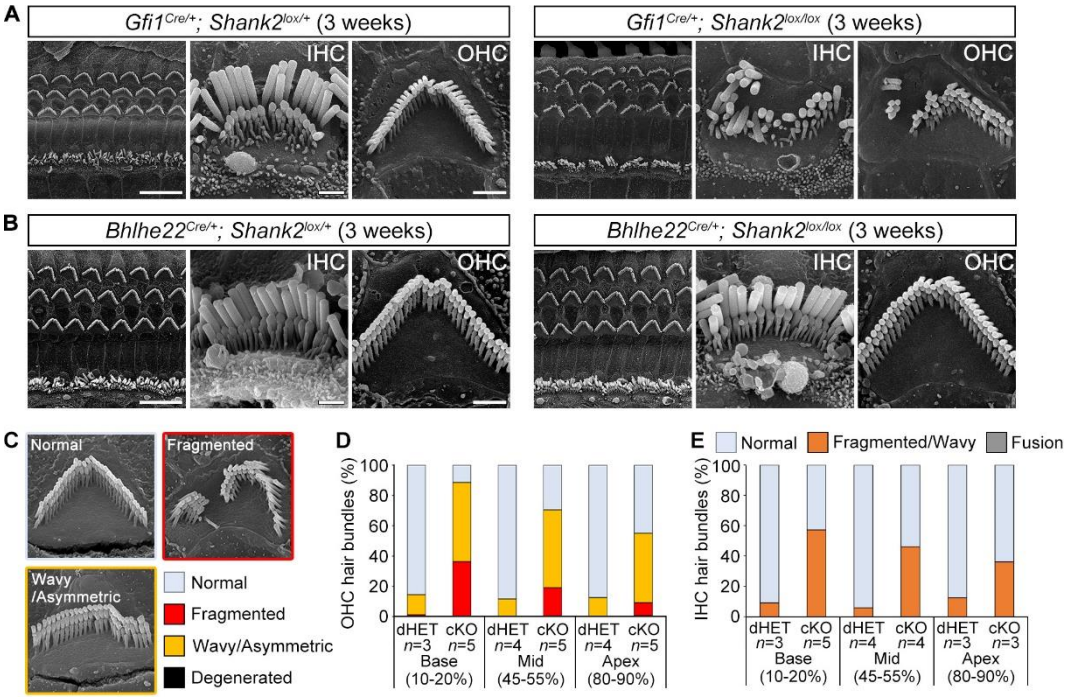


**Fig 13. SHANK2 in hair cells, but not in spiral ganglion neurons, is essential for stereocilia formation.** (A) SEM images show hair bundle defects in 3-week-old *Gfi1*$^{Cre}$*; Shank2*$^{lox/lox}$ mice. (B) Normal hair bundles are observed in 3-week-old *Bhlhe22*$^{Cre}$*; Shank2*$^{lox/lox}$ mice. (C-E) Examples (C) and proportions of OHC (D) and IHC (E) bundle defects in *Gfi1*$^{Cre}$*; Shank2*$^{lox/lox}$ mice. Scale bars: A-B (low magnification), 10 μm; A-B (IHC/OHC), 1 μm.

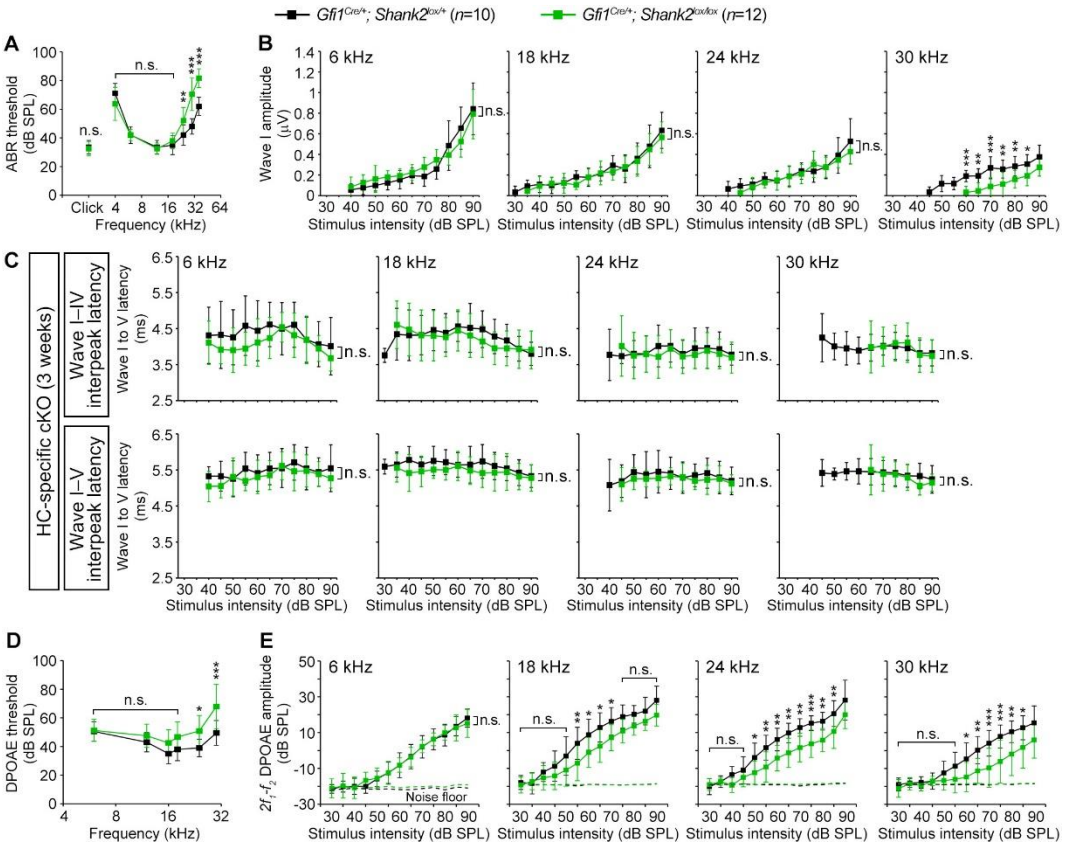


**Fig 14. SHANK2 in hair cells is essential for normal hearing.** (A-E) ABR and DPOAE measurements in 3-week-old *Gfi1*$^{Cre}$*; Shank2*$^{lox/lox}$ mice show that ABR (A) and DPOAE (D) thresholds are elevated at high frequencies in HC-specific *Shank2* mutant mice. (B) I/O functions of ABR wave I amplitudes reveal significant changes at high frequency (30 kHz), but not at lower frequencies. (C) Interpeak latencies between waves I–IV and I–V remained within normal range in HC-specific mutant mice. (E) I/O functions of DPOAE amplitudes show a significant reduction at higher frequencies in *Gfi1*$^{Cre}$*; Shank2*$^{lox/lox}$ mice. Data are presented as means ± standard deviation. Statistical comparisons were performed using two-way ANOVA with Bonferroni correction (n.s., non-significant, *P < 0.05, **P < 0.01, ***P < 0.001).

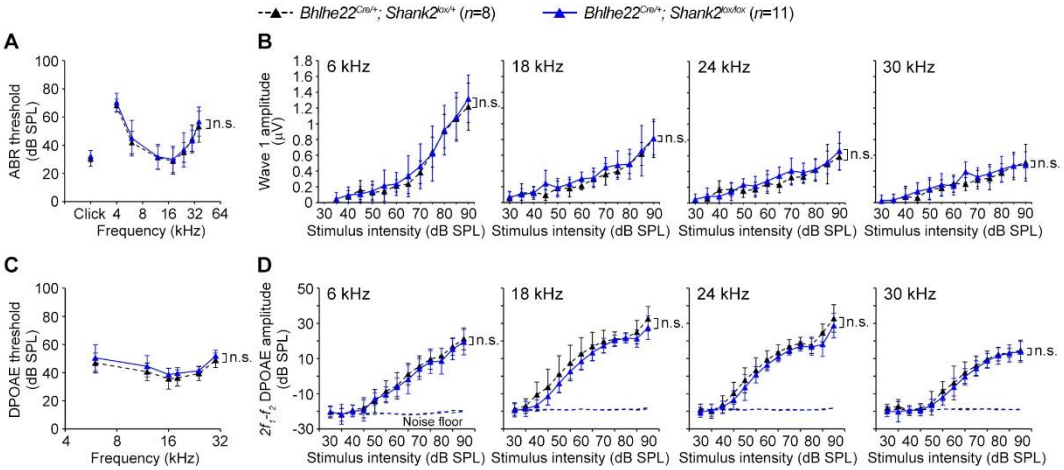


**Fig 15. SHANK2 in spiral ganglion neurons is not required for normal hearing.** (A-D) ABR and DPOAE measurements in 3-week-old *Bhlhe22$^{Cre}$; Shank2$^{lox/lox}$* mice show that ABR (A) and DPOAE (C) thresholds are comparable to control (*Bhlhe22$^{Cre}$; Shank2$^{lox/+}$*) mice. (B) I/O functions of ABR wave I amplitudes reveal no significant changes in SGN-specific *Shank2* mutant. (D) I/O functions of DPOAE amplitudes show normal OHC function in *Bhlhe22$^{Cre}$; Shank2$^{lox/lox}$* mice. Data are presented as means ± standard deviation. Statistical comparisons were performed using two-way ANOVA with Bonferroni correction (n.s., non-significant).

### 3.5. Hair bundle integrity and hearing function progressively decline with age in *Shank2* mutants

To evaluate the long-term effects of disrupted bundle architecture on auditory function, we conducted a longitudinal study measuring ABR and DPOAE thresholds in systemic, HC-specific, and SGN-specific *Shank2* mutants. Measurements were taken monthly for up to 16 weeks. In both systemic and HC-specific *Shank2* mutants, the initial high-frequency shifts in ABR and DPOAE thresholds observed at 3 weeks progressively extended to lower frequencies and increased in magnitude over time (Fig. 16A-D). In contrast, SGN-specific mutants exhibited no significant changes throughout the study period (Fig. 16E-F).

At 16 weeks, we observed significant hair bundle degeneration in systemic and HC-specific *Shank2* mutants, but not in SGN-specific mutants (Fig. 17A), which aligned with the progressive decline in hearing function (Fig. 16). OHC hair bundle loss exceeded 80% in the basal region, while it remained below 10% in the middle and apical regions (Fig. 17C-D). IHCs displayed moderate bundle loss at the basal turn of the cochlea, but little in the middle and apical turns (Fig. 17E-F). These results suggest that the loss of the U- or V-shaped bundle architecture makes hair bundles more prone to significant degeneration over time. Interestingly, there was no direct correlation between the frequencies with threshold shifts and the tonotopic regions showing hair bundle degeneration. For example, despite significant threshold shifts at 18 kHz (Fig. 16A-D), no substantial bundle degeneration was observed in the corresponding tonotopic region (45-55% from the basal end) (Fig. 17C-F) [38,39]. This discrepancy implies that hair bundle degeneration alone does not fully explain the progressive hearing loss observed in *Shank2* mutants.

To understand the cause of progressive hearing loss in older *Shank2* mutant mice, we analysed auditory nerve responses at 16 weeks, which were minimally affected at 3 weeks (Figs. 10B and 14B). In systemic and HC-specific *Shank2* mutants (Fig. 18A-B), but not in SGN-specific mutants (Fig. 18C), ABR wave I amplitudes at mid-to-high frequencies (18 and 24 kHz) were significantly reduced at 16 weeks. Additionally, DPOAE amplitudes at these frequencies were also markedly diminished in systemic and HC-specific mutants (Fig. 19A-C). These findings indicate that disruption of the U- or V-shaped hair bundle architecture results in long-term deterioration of auditory nerve responses and OHC function, leading to progressive hearing loss in aged *Shank2* mutants with altered hair bundle morphology.

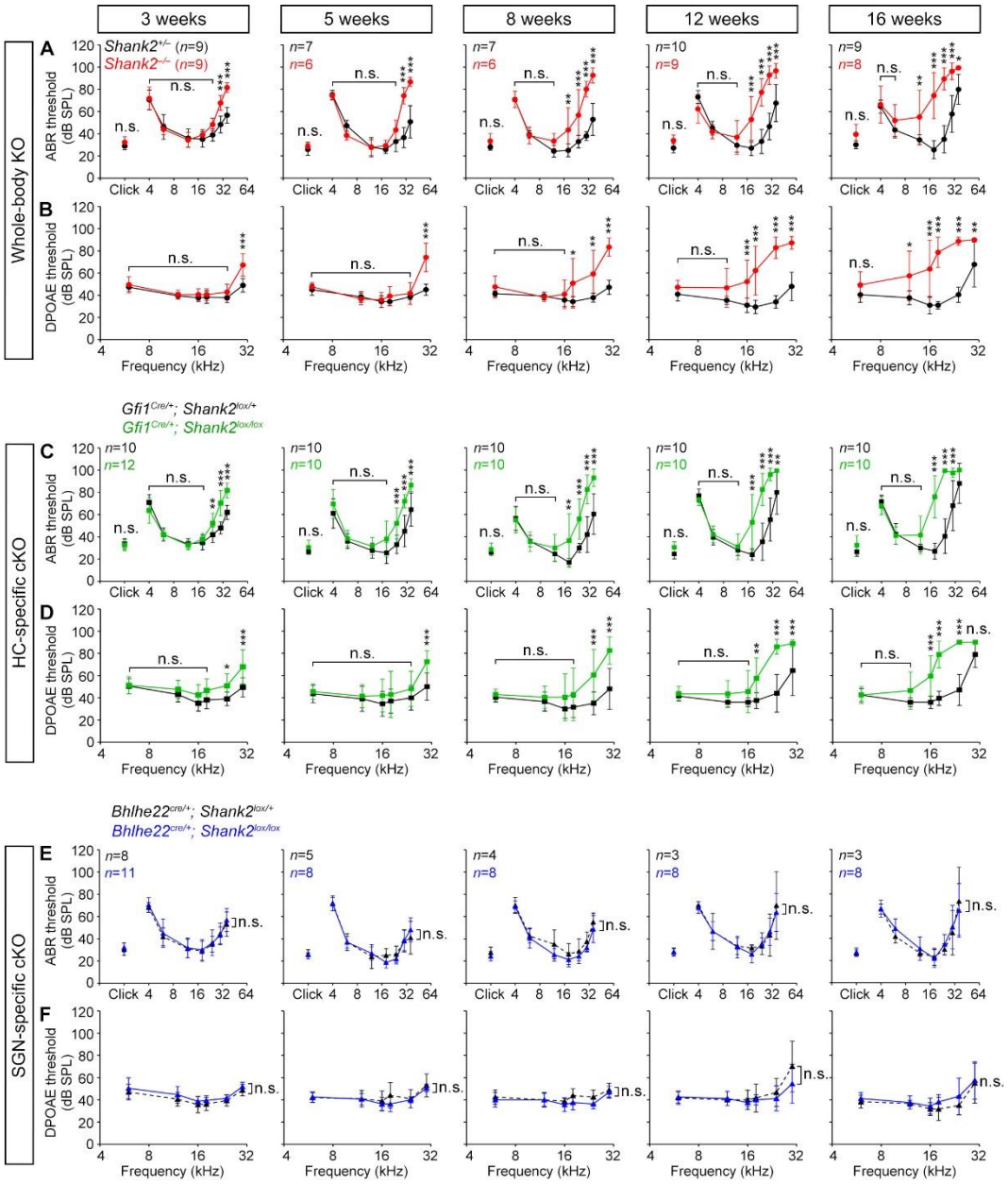


**Fig 16. Long-term analysis of ABR and DPOAE measurements in *Shank2* mutants.** Threshold measurements for ABR and DPOAE were taken at 3, 5, 8, 12, and 16 weeks of age in *Shank2*$^{-/-}$ (A-B), *Gfi1*$^{Cre}$*; Shank2*$^{lox/lox}$ (C-D), and *Bhlhe22*$^{Cre}$*; Shank2*$^{lox/lox}$ (E-F) mice. High-frequency threshold shifts observed at 3-week-old systemic (*Shank2*$^{-/-}$) and HC-specific (*Gfi1*$^{Cre}$*; Shank2*$^{lox/lox}$) *Shank2*

mutnat mice progressively worsen over time, extending to mid-frequencies and increasing in severity. Data are shown as means ± standard deviation. Statistical comparisons were conducted using two-way ANOVA with Bonferroni correction (n.s., non-significant, *P < 0.05, **P < 0.01, ***P < 0.001).

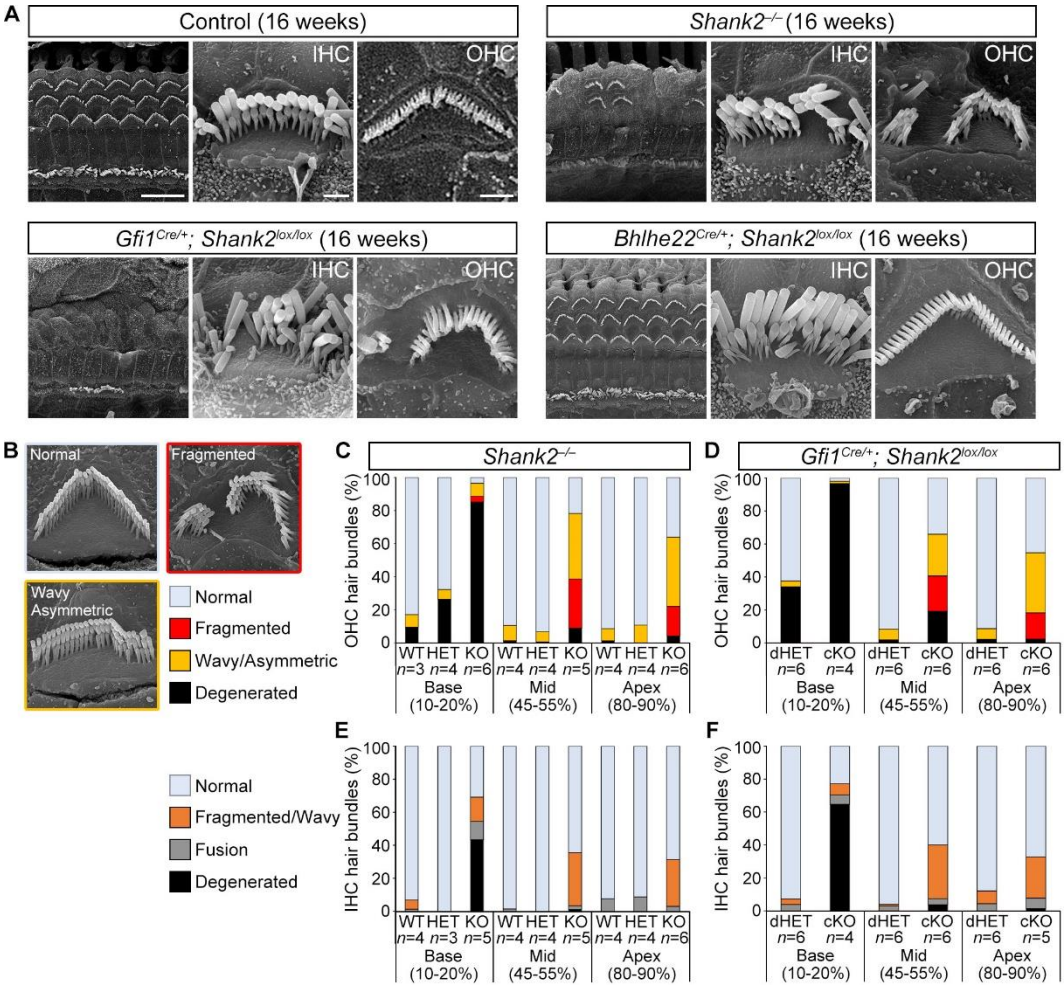


**Fig 17. Degeneration of stereocilia in *Shank2* mutants.** (A) SEM images demonstrate severe hair bundle degeneration in *Shank2*$^{-/-}$ and *Gfi1*$^{Cre}$*; Shank2*$^{lox/lox}$ mice, while *Bhlhe22*$^{Cre}$*; Shank2*$^{lox/lox}$ mice show minimal degeneration. (B-F) Examples (B) and proportions of OHC and IHC bundle defects in 16-week-old *Shank2*$^{-/-}$ (C and E) and *Gfi1*$^{Cre}$*; Shank2*$^{lox/lox}$ (D and F). Scale bars: A (low magnification), 10 μm; A (IHC/OHC), 1 μm.

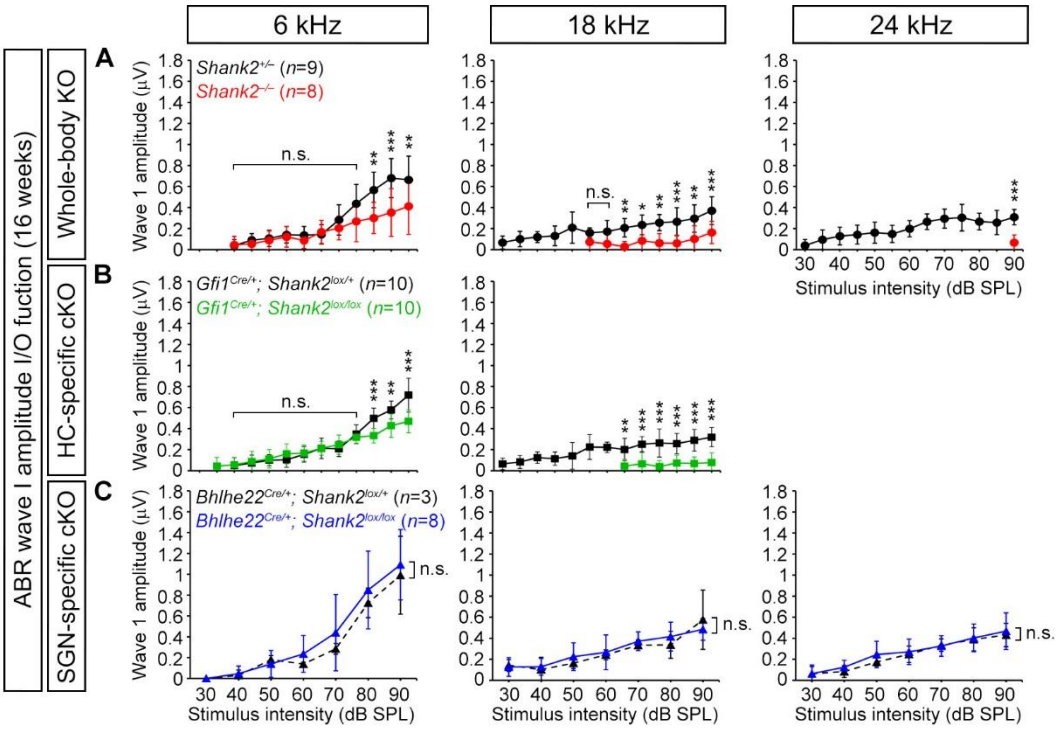


**Fig 18. ABR wave I amplitude analysis at 16 weeks.** (A-C) ABR wave I amplitudes are significantly reduced at mid to high frequencies in systemic (A) and HC-specific (B) *Shank2* cKO mice, but not in SGN-specific (C) *Shank2* cKO mice. Data are shown as means ± standard deviation. Statistical comparisons were made using two-way ANOVA with Bonferroni correction (n.s., non-significant, *P < 0.05, **P < 0.01, ***P < 0.001).

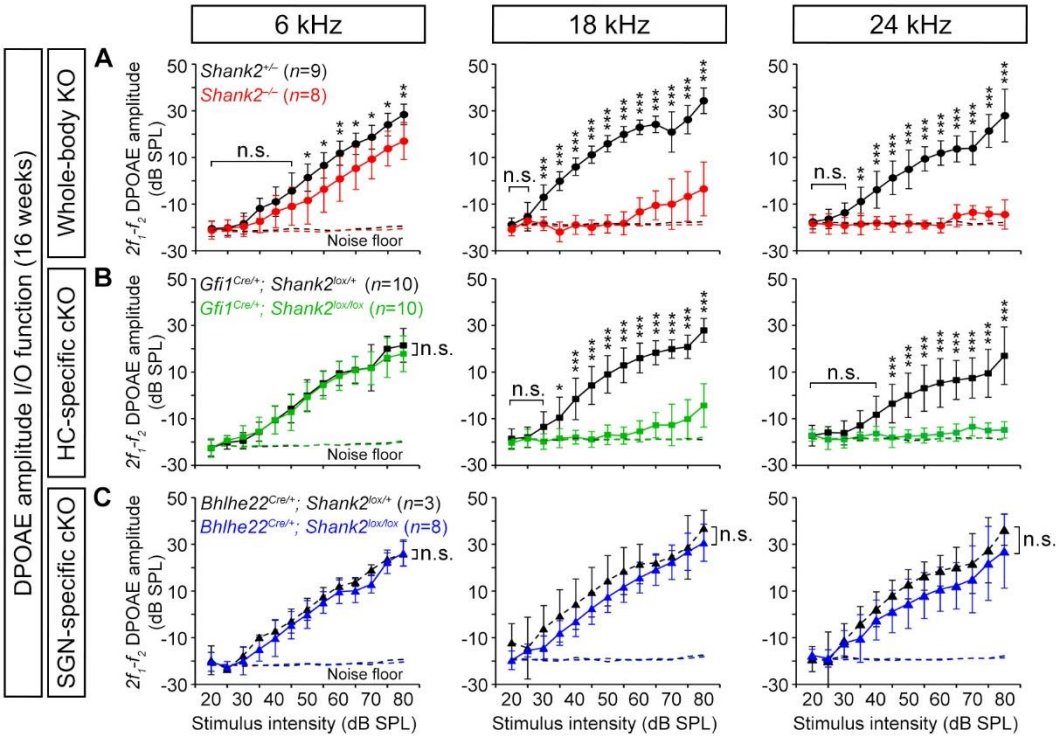


**Fig 19. DPOAE I/O function analysis in 16-week-old *Shank2* mutnats.** (A-C) DPOAE amplitudes are notably decreased at mid to high frequencies (18 and 24 kHz) in systemic (A) and HC-specific (B) *Shank2* cKO mice, but not in SGN-specific (C) *Shank2* cKO mice. Data are shown as means ± standard deviation. Statistical comparisons were made using two-way ANOVA with Bonferroni correction (n.s., non-significant, *P < 0.05, **P < 0.01, ***P < 0.001).

### 3.6. SHANK2 acts independently of known regulators in the establishment of hair bundle architecture

Gαi and GPSM2, which are restricted on the lateral surface of developing hair cells, are crucial for hair bundle morphogenesis [4,5,14]. Their absence results in fragmented or wavy stereociliary bundles, similar to the phenotypes observed in *Shank2* mutants [4,5], and disrupts the mediolateral compartments by causing medial proteins, such as aPKCζ and PARD6B, to encroach into the lateral compartment [5,14]. aPKC has been shown to interact with SHANK2 to establish epithelial cell polarity in intestinal cells [40]. We therefore investigated the relationship between SHANK2 and these known regulators to explore their potential involvement in SHANK2's role in hair bundle formation.

In *Shank2*$^{-/-}$ mutant HCs, although medial SHANK2 expression was absent (Fig. 20A-B, asterisk), the lateral expressions of Gαi and GPSM2 and the medial expressions of aPKCζ and PARD6B remained intact (Fig. 20C-D). Moreover, in *Gpsm2*$^{-/-}$ mutants, where aPKCζ expression was expanded laterally and Gαi expression was reduced (Fig. 21A), the medial localization of SHANK2 was not affected (Fig. 21B). These findings suggest that SHANK2 does not influence the localization of other known medial and lateral regulators and operates independently in hair bundle morphogenesis.

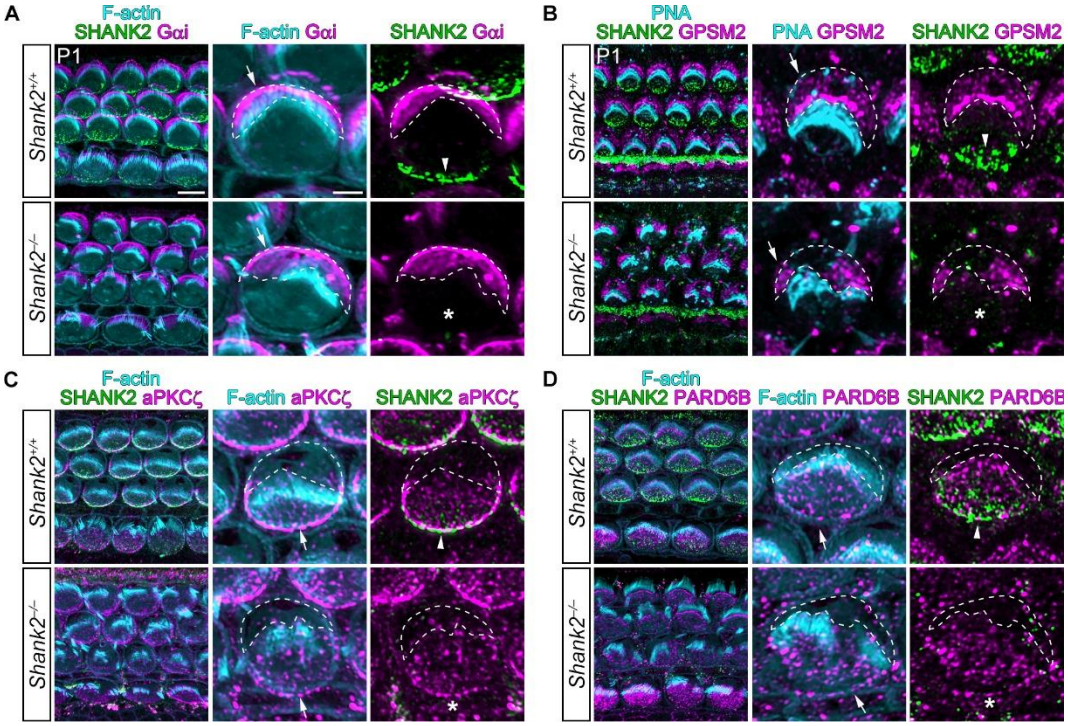


**Fig 20. SHANK2 do not regulate other medial or lateral proteins.** (A-D) Immunostaining for actin filaments (phalloidin or PNA, cyan), SHANK2 (green), and lateral and medial proteins (magenta) in P1 wild-type and *Shank2*$^{-/-}$ mice. In *Shank2*$^{-/-}$ HCs, lateral proteins Gαi (A, arrows) and GPSM2 (B, arrows) maintain their localization in the bare zone (white dashed lines), whereas SHANK2 expression on the medial surface (arrowheads) is absent (asterisks). Similarly, the medial proteins aPKCζ (C, arrows) and PARD6B (D, arrows) retain their localization in *Shank2*$^{-/-}$ HCs, where SHANK2 expression is missing (asterisks). Scale bars: A-D (left panels), 5 μm; middle/right panels, 2 μm.

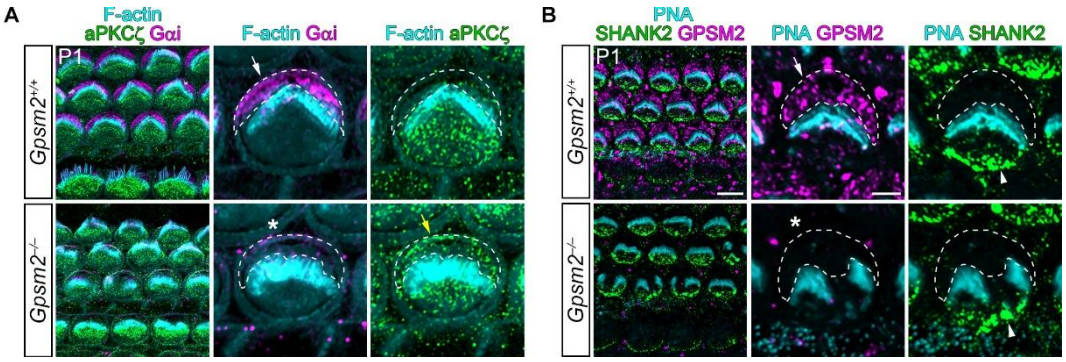


**Fig 21. SHANK2 is not regulated by the lateral component, GPSM2.** (A-B) Immunostaining for actin filaments (phalloidin or PNA, cyan), SHANK2, and lateral and medial proteins in P1 wild-type and *Gpsm2*$^{-/-}$ mice. In *Gpsm2*$^{-/-}$ mice, Gαi (A, arrow) is reduced in the bare zone (asterisk), and aPKCζ extends into the bare zone (yellow arrow). SHANK2 expression is preserved on the medial surface (B, arrowheads) in *Gpsm2*$^{-/-}$ HCs, whereas GPSM2 expression is absent from the bare zone (asterisk). Scale bars: A-B (left panels), 5 μm; middle/right panels, 2 μm.

## 3.7. *Shank2* mutation–induced hair bundle defects are not attributable to structural deficits in the cuticular plate or apical junction

### 3.7.1. Cuticular plate remains intact despite bundle abnormalities in *Shank2* mutants

As the loss of SHANK2 did not alter the distribution of known medial or lateral regulators, we investigated whether other structural features of the hair cell apical surface—specifically the cuticular plate and tight junctions—could be involved in the bundle defects observed in *Shank2* mutants [41,42]. Immunolabeling for LMO7 and β-spectrin, two well-known cuticular plate markers [42,43], revealed continuous and well-defined staining beneath the stereocilia in both control and *Shank2*$^{-/-}$ cochleae, regardless of hair bundle morphology (Fig. 22), suggesting that the overall integrity of the cuticular plate was maintained.

### 3.7.2. Bundle defects in *Shank2* mutants occur independently of apical junction integrity

To evaluate apical junctional integrity, we performed ZO-1 immunostaining. At P1, when bundle defects were already apparent, *Shank2*$^{-/-}$ hair cells exhibited circumferential ZO-1 labeling similar to that of controls (Fig. 23A). By 3 weeks of age, the majority of hair cells retained intact ZO-1 staining, though occasional irregularities in cell borders were observed in outer hair cells with severely disrupted bundles (Fig. 23B). These findings collectively indicate that the bundle defects observed in *Shank2* mutants are unlikely to result from abnormalities in either cuticular plate structure or apical junctional organization.

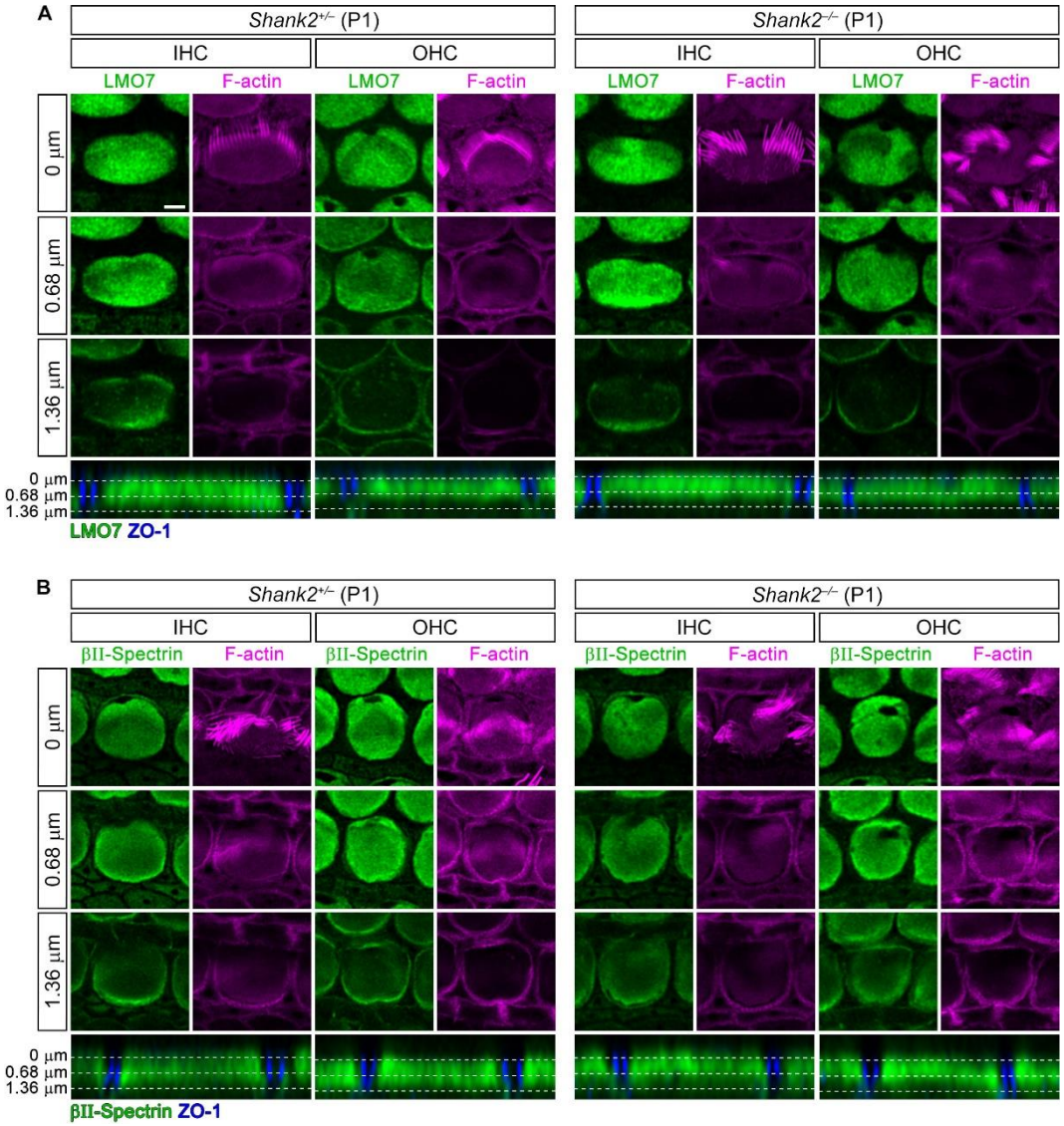


**Fig 22. The cuticular plate remains intact in the cochlea of *Shank2*$^{-/-}$ mice.** (A-B) Representative confocal images show immunostaining for LMO7 (A) and β-Spectrin (B) along with F-actin in cochlear hair cells, presented as 2D projections at different z-planes. Corresponding side-view (xz-plane) images of the same cells are shown with ZO-1 and LMO7 (A), and ZO-1 and β-Spectrin (B). White dashed lines indicate the approximate z-positions of the 2D projections. Scale bars: 2 µm.

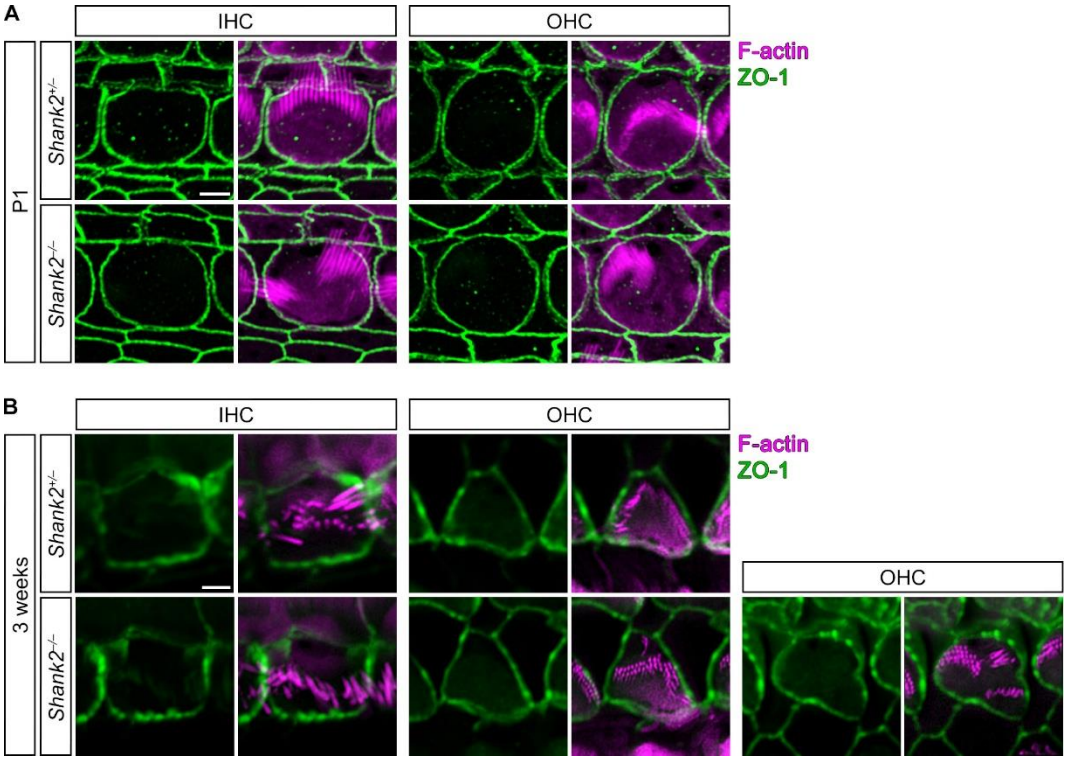


**Fig 23. Apical circumference is maintained in *Shank2*$^{-/-}$ cochlear hair cells.** (A-B) Cochleae were immunostained for ZO-1 and F-actin. (A) At P1, although *Shank2*$^{-/-}$ hair bundles are disorganized, the apical circumference remains comparable to that of *Shank2*$^{+/-}$ mice. (B) By 3 weeks of age, most IHCs and OHCs retain a normal apical circumference, with only minor contour irregularities observed in some OHCs exhibiting severe bundle defects. Scale bars: 2 μm.

## 3.8. RAP1, identified as a potential binding partner of SHANK2, is essential for normal hair bundle morphogenesis

### 3.8.1. RAP1 is a potential interacting partner of SHANK2

Since SHANK2 does not regulate or get regulated by known proteins in the lateral or medial proteins, we investigated potential SHANK2 interacting partners in developing hair cells using yeast two-hybrid screening. SHANK2 proteins possess multiple domains, and alternative splicing produces various isoforms with different domain structures (Fig. 24A) [35,44]. qPCR analysis revealed that *Shank2e*, which includes the N-terminal SPN-ANK domain, is the predominant isoform in the organ of Corti (Fig. 24B). The SPN-ANK domain of SHANK2E has been elucidated to be essential for its localization at cell-cell contact sites and tight junction formation in kidney epithelial cells [40]. Therefore, we selected the SPN-ANK domain as the bait for our screening, using cDNA libraries from mouse inner ears at E16.5 and P2-P6, representing the onset and completion of hair bundle morphogenesis. This screening identified RAS-related protein 1B (RAP1B) as a potential binding partner for SHANK2, with the highest confidence scores in both cDNA libraries (Table 1 and 2). Previous studies have corroborated our findings, showing that RAP1 interacts with the SPN-ANK domain of SHANK proteins and is crucial for regulating the morphology and stability of actin-based cytoskeletal structures in osteosarcoma cells. Inhibition of RAP1 leads to disrupted tight junctions and mislocalization of polarity proteins in kidney epithelial cells [40,45].

### 3.8.2. RAP1 is crucial for normal hair bundle morphogenesis

To explore the role of RAP1 in hair bundle morphogenesis, we performed organ of Corti explant cultures from E14.5 mouse embryos with the RAP1 inhibitor GGTI298 for six days *in vitro* (DIV) [40]. Control explants displayed the typical U- and V-shaped stereociliary bundles after 6 DIV (Fig. 25A). In contrast, explants treated with the RAP1 inhibitor exhibited a loss of normal hair bundle architecture, showing severe fragmentation similar to the abnormalities observed in *Shank2*$^{-/-}$ mutants (Fig. 25B). These results indicate that RAP1, a potential binding partner of SHANK2, is crucial for proper hair bundle morphogenesis.

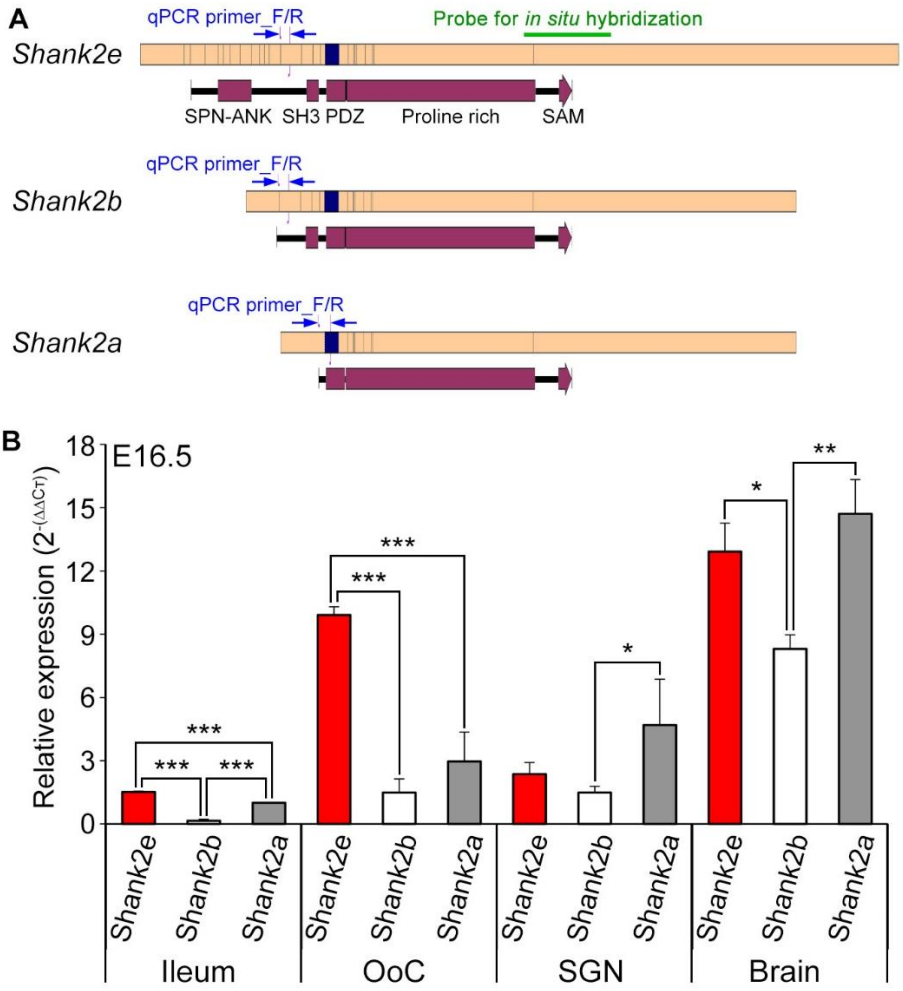


**Fig 24. Expression of *Shank2* isoforms in the mouse cochlea.** (A) Schematic diagram of mouse *Shank2* isoforms. The mRNA structure is illustrated with exons (upper bars), and deleted regions in *Shank2* mutants are highlighted as dark blue boxes. Locations of qPCR primers (blue arrows) and the *in situ* hybridization probe (green bar) are marked. Corresponding SHANK2 protein domains are depicted below. (B) Quantitative real-time PCR analysis of *Shank2* isoforms in the ileum, organ of Corti (OoC), spiral ganglion neuron (SGN), and brain. *Shank2e* (red) is the predominant isoform in the organ of Corti at E16.5, similar to its expression in the ileum. In contrast, *Shank2a* (gray) is most abundantly expressed in SGNs and shows similar expression levels in the brain. Data are shown as means ± standard deviation. Statistical comparisons were performed using one-way ANOVA with

Tukey correction for multiple comparisons (n.s., non-significant, *P < 0.05, **P < 0.01, ***P < 0.001).

**Table 1. Candidate interacting partners of SHANK2 identified by yeast two-hybrid screening using a cDNA library from inner ears dissected at E16.5**

| Gene symbol | Gene name | Accession No. | Score |
|---|---|---|---|
| Rap1b | RAS related protein 1b | NM_024457.2 | A |
| Gnai3 | G protein subunit alpha i3 | NM_010306.3 | A |
| Gnas var10 | Guanine nucleotide binding protein, alpha stimulating complex locus, transcript variant 10 | NM_001310083.1 | A |
| Ap3b1 | Adaptor-related protein complex 3, beta 1 subunit | NM_009680.3 | B |
| Hras1 | Harvey rat sarcoma virus oncogene 1, transcript variant 1 | NM_008284.2 | B |
| Nras | Neuroblastoma ras oncogene | NM_010937.2 | B |
| Rap2a | RAS related protein 2a | NM_029519.3 | B |
| Tbc1d23 var1 | TBC1 domain family, member 23, transcript variant 1 | NM_001358433.1 | B |
| Gnas var8 | Guanine nucleotide binding protein, alpha stimulating complex locus, transcript variant 8 | NM_001077510.5 | C |
| Cdon | Cell adhesion molecule-related/down-regulated by oncogenes | NM_021339.2 | D |
| Ednrb | Endothelin receptor type B, transcript variant 3 | NM_001276296.1 | D |
| Kif17 | Kinesin family member 17, transcript variant 2 | NM_001190978.1 | D |
| Kras | Kirsten rat sarcoma viral oncogene homolog | NM_021284.6 | D |
| Nnat | Neuronatin, transcript variant 2 | NM_180960.3 | D |
| Patz1 | POZ (BTB) and AT hook containing zinc finger 1, transcript variant 1 | NM_019574.3 | D |
| Rap1a | RAS-related protein 1a | NM_145541.5 | D |
| Rap2b | member of RAS oncogene family | NM_028712.4 | D |
| Rgl3 | Ral guanine nucleotide dissociation stimulator-like 3 | NM_023622.4 | D |
| Zfp62 | Zinc finger protein 62, transcript variant 5 | NM_001362727.1 | D |

**Table 2. Candidate interacting partners of SHANK2 identified by yeast two-hybrid screening using a cDNA library from inner ears dissected at P2-P6**

| Gene symbol | Gene name | Accession No. | Score |
|---|---|---|---|
| Rap1b | RAS related protein 1b | NM_024457.2 | A |
| Gnas var10 | Guanine nucleotide binding protein, alpha stimulating complex locus, transcript variant 10 | NM_001310083.1 | A |
| Gnas var8 | Guanine nucleotide binding protein, alpha stimulating complex locus, transcript variant 8 | NM_001077510.5 | B |
| Ap3b1 | Adaptor-related protein complex 3, beta 1 subunit | NM_009680.3 | D |
| Hras1 | Harvey rat sarcoma virus oncogene 1, transcript variant 1 | NM_008284.2 | D |
| Kansl1 | KAT8 regulatory NSL complex subunit 1, transcript variant 5 | NM_001372460.1 | D |
| Ppp2r5c | Protein phosphatase 2, regulatory subunit B', gamma, transcript variant 17 | NM_001373950.1 | D |
| Rap2b | RAP2B, member of RAS oncogene family | NM_028712.4 | D |
| Rras | related RAS viral oncogene, transcript variant 1 | NM_009101.3 | D |

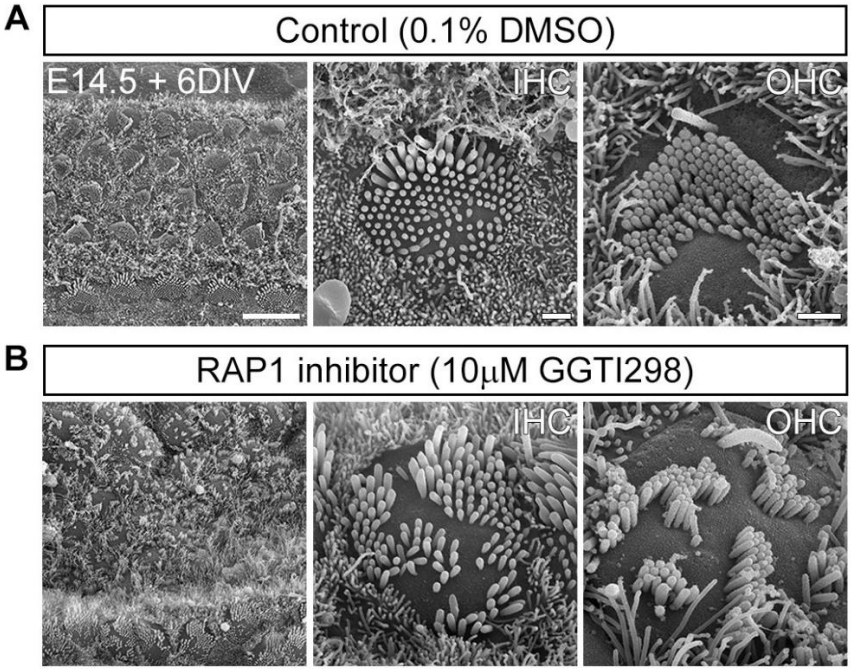


**Fig 25. RAP1 inhibition disrupts hair bundle architecture.** (A-B) SEM images of stereociliary bundles from E14.5 organ of Corti explants cultured for 6 days in vitro (DIV) show that hair bundles, which normally have a U- or V-shape (A), become randomly fragmented in explants treated with the RAP1 inhibitor (GGTI298) (B). Scale bars: A-B (left panels), 10 μm; IHC/OHC, 1 μm.

### 3.8.3. RAP1 modulates the medial localization of SHANK2 in developing hair cells

Given that SHANK2 deficiency (*Shank2*$^{-/-}$) and RAP1 inhibition both result in similar hair bundle defects, we explored whether RAP1 influences hair bundle morphogenesis by regulating the medial localization of SHANK2. In control explants, SHANK2 was localized to the medial domain in both IHCs and OHCs (Fig. 26A, arrowheads). However, this medial localization of SHANK2 was lost in explants treated with the RAP1 inhibitor (Fig. 26B, asterisks). In contrast, the localization of other medial proteins, such as aPKCζ and PARD6B, remained unchanged (Fig. 27A-B). Similarly, RAP1 inhibition did not affect the localization of lateral proteins such as GPSM2 and Gαi (Fig. 27C-D). These data indicate that RAP1's role in hair bundle morphogenesis is specifically related to regulating the medial localization of SHANK2, without impacting the overall mediolateral compartmentalization.

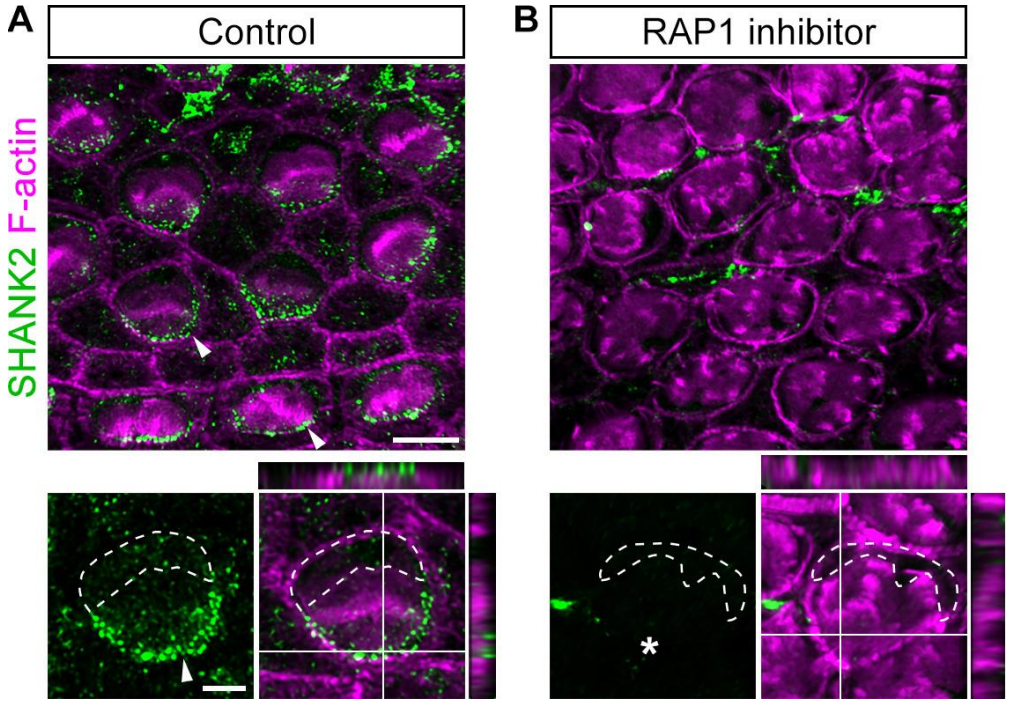


**Fig 26. RAP1 regulates the localization of SHANK2 in auditory hair cells.** (A-B) In RAP1 inhibitor-treated explants, SHANK2 on the medial surface (arrowhead) is absent, and hair bundles lose their characteristic structure (asterisk). The boundaries between hair cells and supporting cells become disorganized. Scale bars: A-B (upper panels), 5 μm; lower panels, 2 μm.

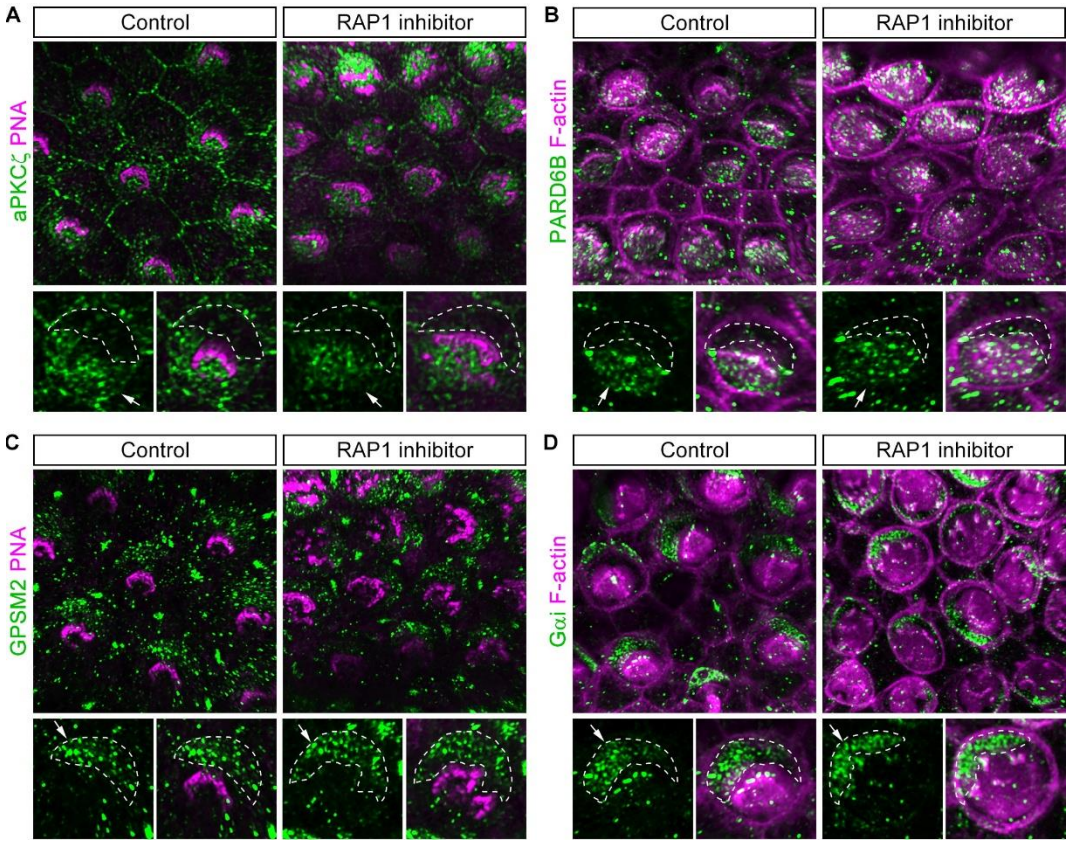


**Fig 27. RAP1 inhibition does not affect the distribution of other medial/lateral proteins.** (A-D) Despite the treatment with RAP1 inhibitor, medial expression of aPKCζ (A) and PARD6B (B), as well as lateral expression of GPSM2 (C) and Gαi (D), are preserved (arrows). Scale bars: A-D (upper panels), 5 μm; lower panels, 2 μm.

## 3.9. RAP1, identified as a potential binding partner of SHANK2, is essential for normal hair bundle morphogenesis

### 3.9.1. RAP1 is essential for proper SHANK2 localization in developing hair cells *in vivo*

Although GGTI298 has been reported to inhibit RAP1, it also affects other small G-proteins such as RhoA [40,46], and the use of explant cultures limits the ability to fully assess the functional consequences of RAP1 inhibition. To specifically examine the role of RAP1 *in vivo*, we generated two conditional knockout (cKO) models targeting both *Rap1a* and *Rap1b*, given their known functional redundancy [47]. The first was an otic-specific cKO (*Slc26a9*$^{Cre}$*; Rap1a*$^{lox/lox}$*; Rap1b*$^{lox/lox}$), which deletes both genes from the otocyst starting at E9.5 [21], and the second was a hair cell–specific cKO (*Gfi1*$^{Cre}$*; Rap1a*$^{lox/lox}$*; Rap1b*$^{lox/lox}$), which ablates *Rap1a* and *Rap1b* in differentiating hair cells beginning at E15.5 [18].

In otic-specific *Rap1* mutants, medial localization of SHANK2 (Fig. 28A-B, arrowhead) was completely absent in both hair cell types at E16.5 and P1 (Fig. 28A-B, asterisks). These mutants also displayed severely fragmented hair bundles and disrupted organ of Corti organization (Fig. 28A-B). In contrast, hair cell–specific *Rap1* mutants initially exhibited medial SHANK2 localization at E16.5 (Fig. 28°, yellow arrowhead), which was lost by P1 (Fig. 28B, asterisk), likely due to the later onset of *Rap1* deletion driven by *Gfi1*$^{Cre}$, occurring after SHANK2 localization begins. In both models, mislocalized SHANK2 formed cytoplasmic aggregates at P1 (Fig. 28B), suggesting that SHANK2 protein expression is preserved despite its abnormal localization. Consistent with explant data (Fig. 27), both *Rap1* mutants retained normal medial aPKCζ and lateral Gαi distribution (Fig. 28C-D, arrows). Additionally, similar to *Shank2* mutants (Fig. 7), kinocilium formation and positioning, assessed using ARL13B staining, remained unaffected in HC-specific *Rap1* mutants, indicating that RAP1 is not required for kinocilium morphogenesis or migration in developing hair cells (Fig. 29A-B). Together, these findings indicate that RAP1 plays a specific role in directing and maintaining the medial localization of SHANK2 during hair cell development.

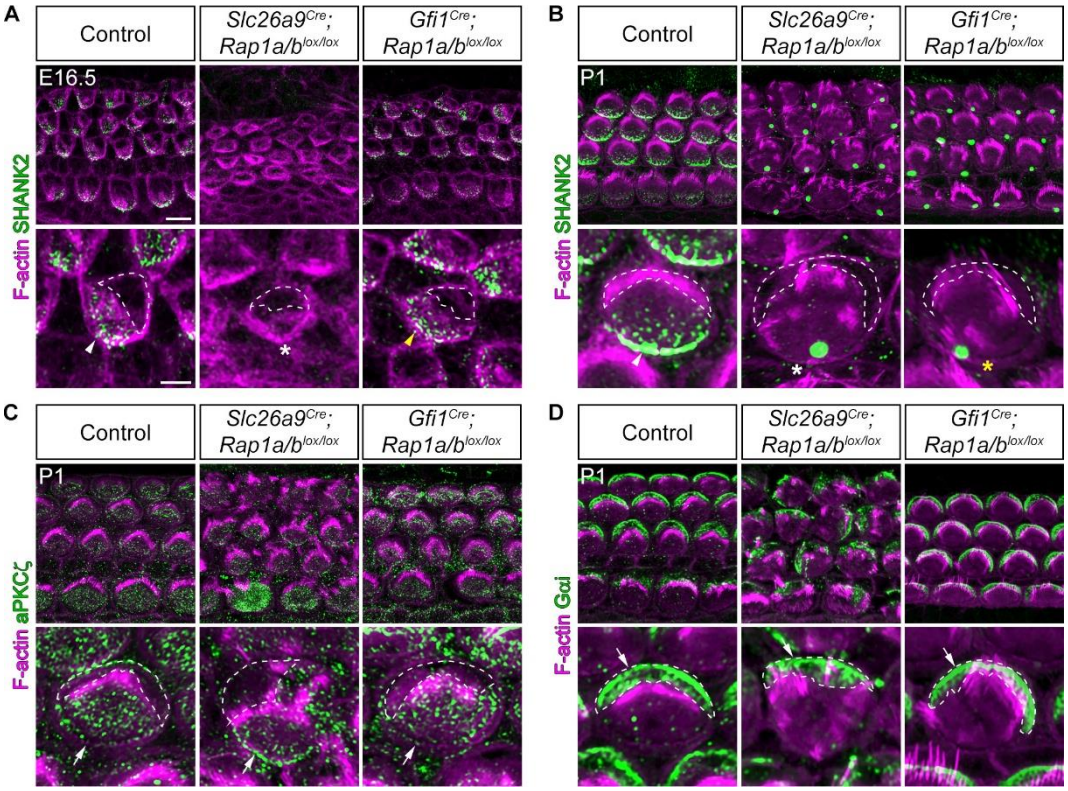


**Fig 28. RAP1 localizes SHANK2 to the medial apical surface without altering other medial/lateral proteins.** (A-B) SHANK2 localization in *Rap1* mutant cochleae. At E16.5, SHANK2 is localized to the medial apical surface in both control and HC-specific (*Gfi1*$^{Cre}$*; Rap1a/b*$^{lox/lox}$) mutants (A, arrowheads), but is absent in otic-specific (*Slc26a9*$^{Cre}$*; Rap1a/b*$^{lox/lox}$) mutants (A, asterisk). By P1, SHANK2 remains medially localized in controls (B, arrowhead), but is lost in both mutant lines (B, asterisks). (C–D) Despite the loss of SHANK2, both *Rap1* mutants retain medial localization of aPKCζ (C, arrows) and lateral localization of Gαi (D, arrows). Scale bars: A-D (low magnification), 5 μm; A-D (high magnification), 2 μm.

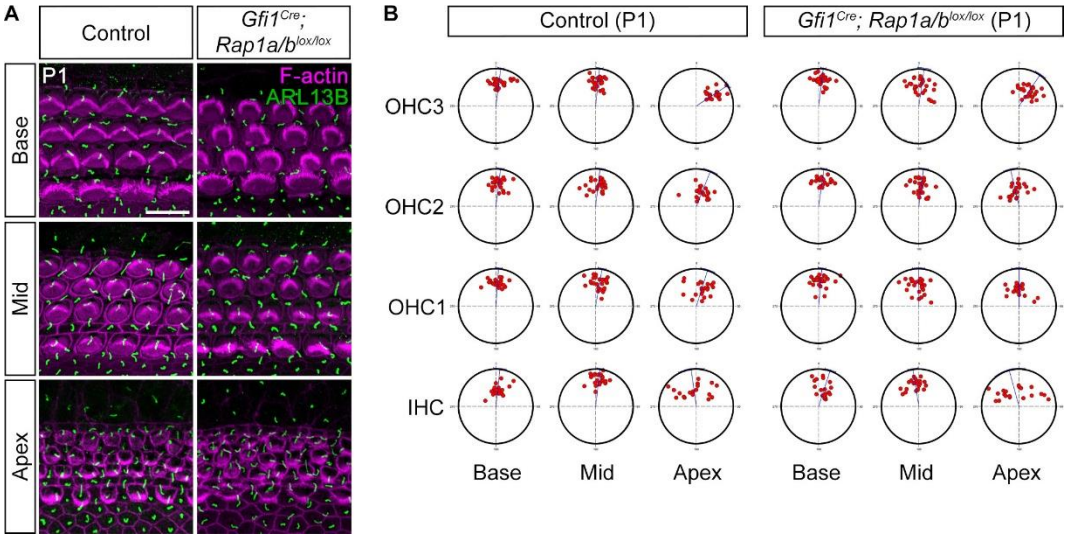


**Fig 29. RAP1 is not essential for the kinocilium development and migration.** (A) Immunostaining with anti-ARL13B (green) antibody shows that kinocilium development is normal in HC-specific *Rap1* mutant. (B) Circular histograms plot the position of the basal body marked as anti-γ-Tubulin antibody. Basal body positioning in *Gfi1*$^{Cre}$*; Rap1a/b*$^{lox/lox}$ cochlea (n = 3) is comparable to that in control cochlea (n = 3). Scale bars: A, 10 μm.

### 3.9.2. *Rap1*-deficiency in hair cells disrupts hair bundle architecture and high-frequency hearing

We next investigated how SHANK2 mislocalization in *Rap1* cKO mutants influences hair bundle morphology. In otic-specific *Rap1* mutants, hair bundles were severely disrupted by 3 weeks of age, displaying fragmented structures and a complete loss of the typical linear or V-shaped configuration (Fig. 30A). These mutants also showed a disorganized organ of Corti and extensive degeneration of outer hair cells (OHCs), with total loss in the apical region and only two remaining rows in the mid-to-basal cochlear turns (Fig. 30A). In contrast, HC-specific *Rap1* mutants exhibited milder abnormalities, primarily characterized by U-shaped rather than V-shaped OHC bundles along the cochlear duct (Fig. 30A). To quantify these morphological differences, we calculated the ratio between the triangular area—formed by connecting the bundle's vertex and endpoints—and the actual bundle area (Fig. 30B). While control OHCs maintained a V-shaped architecture with area ratios close to 1, HC-specific *Rap1* mutants exhibited higher ratios, consistent with a U-shaped bundle morphology (Fig. 30C).

To evaluate auditory function, we assessed both *Rap1* mutant models at 3 weeks, consistent with the timepoint used for analyzing *Shank2* mutants (Fig. 10). Otic-specific *Rap1* mutants exhibited profound hearing loss across all tested frequencies, as determined by both ABR and DPOAE (Fig. 31A). In contrast, HC-specific *Rap1* mutants—characterized by U-shaped OHC bundles—displayed hearing deficits restricted to high frequencies in both ABR and DPOAE measurements (Fig. 31B), closely resembling the phenotype observed in *Shank2* mutants (Fig. 10). DPOAE amplitudes progressively declined with increasing frequency (Fig. 31D), and ABR wave I amplitude was significantly reduced at 30 kHz, but remained unaffected at 18 and 24 kHz (Fig. 31C). Additionally, at 6 kHz, we observed reduced wave I amplitudes under high-intensity stimuli, suggesting that RAP1 may also contribute to auditory function in the apical cochlear region. Collectively, these findings demonstrate that proper hair bundle geometry, maintained by the RAP1–SHANK2 pathway, is critical for OHC–mediated amplification, particularly at high frequencies.

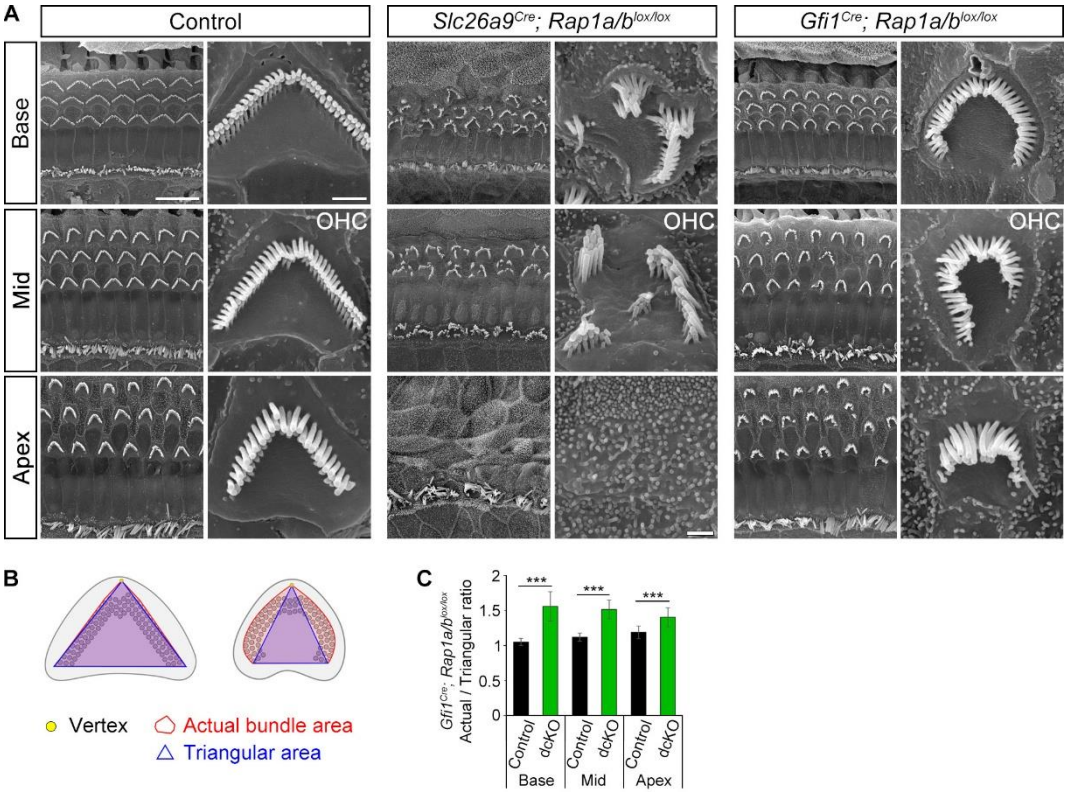


**Fig 30. RAP1 plays a critical role in hair bundle morphogenesis.** (A) SEM images of hair bundles at 3 weeks reveal distinct phenotypes in two different *Rap1* mutants. In controls, OHC bundles exhibit a characteristic V-shape. In contrast, otic-specific *Rap1* mutants show severe bundle fragmentation, with OHCs degenerating into two rows in the middle turn and complete loss in the apical turn. Hair cell-specific *Rap1* mutants display rounded, U-shaped bundles, but without signs of degeneration. (B) Bundle shape was quantified by calculating the ratio of the triangular area (from vertex to bundle ends) to the actual bundle area. (C) Control OHCs exhibited ratios near 1, consistent with their V-shaped structure, while HC-specific *Rap1* mutants showed significantly increased ratios throughout the cochlear duct, reflecting altered bundle morphology. Data are shown as means ± standard deviation. Statistical comparisons were made using two-way ANOVA with Bonferroni correction (n.s., non-significant, *P < 0.05, **P < 0.01, ***P < 0.001). Scale bars: A (low magnificationn), 10 μm; A (high magnification), 1 μm.

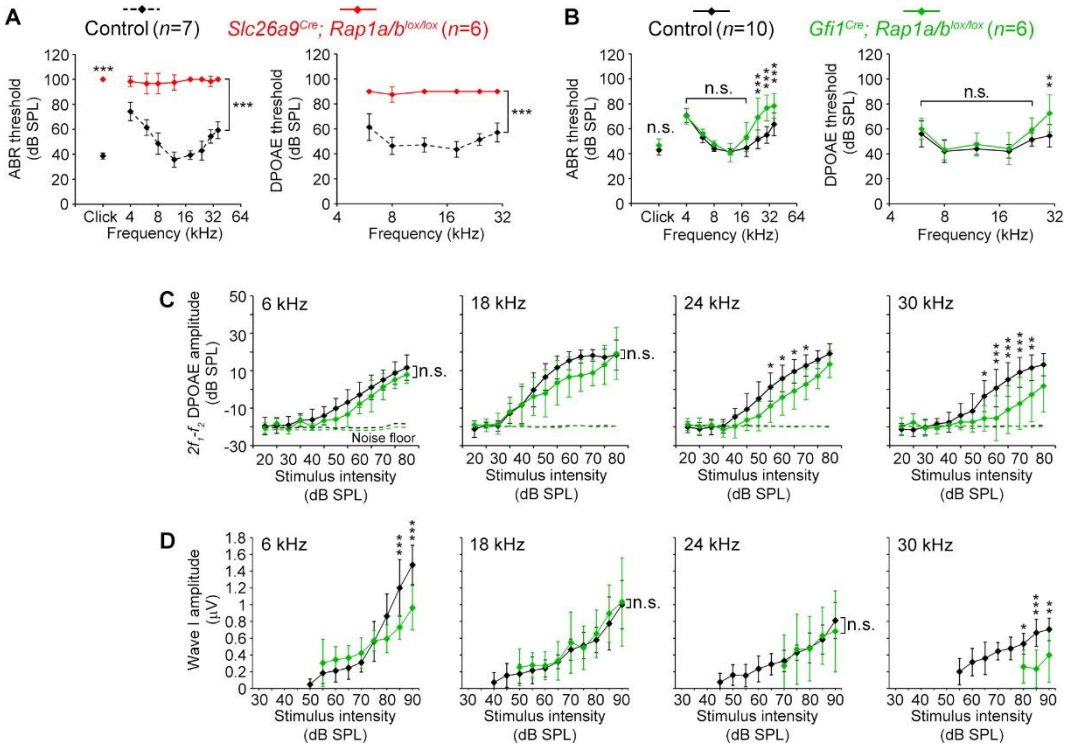


**Fig 31. Loss of RAP1 affects hearing function.** (A-C) Auditory function at 3 weeks shows distinct deficits between two *Rap1* mutant mice. Otic-specific *Rap1* mutants exhibit elevated ABR and DPOAE thresholds across all tested frequencies (A), whereas HC-specific mutants display threshold shifts limited to high frequencies (B), accompanied by a progressive decline in DPOAE amplitudes at higher frequencies (C). (D) Analysis of ABR wave I amplitudes in HC-specific *Rap1* mutants reveals a significant reduction at 30 kHz, with no changes at 18 and 24 kHz, and an additional decrease at 6 kHz observed only at higher stimulus intensities. Data are shown as means ± standard deviation. Statistical comparisons were made using two-way ANOVA with Bonferroni correction (n.s., non-significant, *P < 0.05, **P < 0.01, ***P < 0.001).

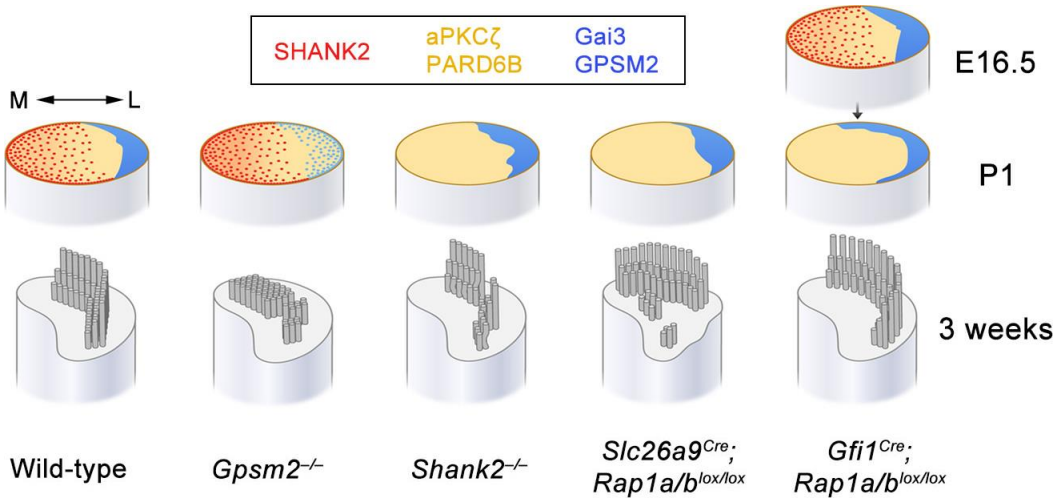


**Fig 32. Summary diagram of protein localization and hair bundle morphology across different mutant backgrounds.** In wild-type cochlear HCs, proteins are properly localized, and OHC bundles exhibit a normal V-shaped architecture. In *Gpsm2*$^{-/-}$ mice, SHANK2 remains medially localized; however, lateral Gαi is reduced and medial aPKCζ expands, leading to numerous short stereocilia and a disrupted staircase pattern. *Shank2*$^{-/-}$ mice lack medial SHANK2 but retain normal localization of medial (aPKCζ, PARD6B) and lateral (Gαi, GPSM2) proteins. These cells display disorganized V-shaped bundle geometry while preserving the staircase arrangement. In both *Rap1* mutant lines, SHANK2 is absent despite preserved medial/lateral polarity protein localization, resulting in bundle abnormalities. Otic-specific *Rap1* mutants (*Slc26a9*$^{Cre}$*; Rap1a/b*$^{lox/lox}$) fail to recruit SHANK2 medially at any stage and exhibit severe bundle defects. In contrast, HC-specific mutants (*Gfi1*$^{Cre}$*; Rap1a/b*$^{lox/lox}$) transiently localize SHANK2 medially but do not maintain it, leading to rounded, U-shaped OHC bundles.

# 4. Discussion

In mammals, auditory HCs have developed distinct bundle structures, such as the V-shaped configuration found in OHCs. In this study, we uncover a molecular pathway that governs the formation of this architecture and highlight its critical role in hearing. SHANK2, acting downstream of the small GTPase RAP1, is restricted to the medial apical surface of developing HCs, where it regulates proper bundle assembly. Through cell type-specific gene knockout approaches, we demonstrate that loss of SHANK2-dependent bundle organization compromises high-frequency hearing by reducing OHC-mediated amplification. Over time, these structural abnormalities lead to progressive degeneration of hair bundles and a decline in auditory sensitivity. Our findings offer key insights into the molecular mechanisms underlying hair bundle development and underscore the functional relevance of the unique bundle configuration in mammals. A comparative overview of protein localization and hair bundle phenotypes across various mutant lines is shown in Fig. 32.

## 4.1. SHANK2, a unique model that regulates only bundle architecture on the medial surface of hair cells

The asymmetric staircase arrangement of stereocilia is regulated by Gαi and GPSM2, which are the earliest proteins to be asymmetrically expressed on the lateral surface of developing hair cells[4,5]. These lateral proteins control the movement of the kinocilium and define the mediolateral boundary. They later migrate to the tips of the stereocilia, facilitating elongation and contributing to the staircase pattern[14,15]. Our study identifies SHANK2 as a key medial counterpart, co-expressed with Gαi, crucial for forming the U- or V-shaped hair bundle architecture (Figs. 2-3, 5 and 8). Unlike mutations in Gαi and GPSM2, which disrupt kinocilium positioning and the staircase arrangement, SHANK2-deficient hair cells maintain these features (Fig. 9). The expression of Gαi/GPSM2 on the lateral surface and aPKCζ/PARD6B on the medial surface remains unchanged (Fig. 20), and the staircase pattern and essential stereociliary components are unaffected in *Shank2* mutants (Fig. 9). These findings suggest that SHANK2 specifically regulates the formation of the U- or V-shaped hair bundle architecture and functions independently of the known medial and lateral proteins. Moreover, the bundle defects observed in *Shank2* mutants are unlikely to result from disruptions of other apical structures. Both the cuticular plate and apical junctions remain structurally intact (Figs.

22-23), and kinocilium formation and positioning are preserved in both *Shank2* and *Rap1* mutants (Figs. 7 and 29). These observations suggest that the bundle abnormalities in *Shank2* mutants are not secondary defects in apical surface architecture.

The exact mechanism by which SHANK2 shapes the unique hair bundle architecture remains to be elucidated. Previous research has demonstrated that SHANK proteins facilitate actin polymerization during spine development and stabilize the actin cytoskeleton in mature neurons[48,49]. Specifically, the proline-rich domain of SHANK2 recruits the actin nucleation-promoting factor cortactin in hippocampal neurons[49]. Additionally, SHANK3 directly binds with actin via its SPN-ANK domain, affecting filopodia formation in osteosarcoma cells and spine morphology in hippocampal neurons[45]. These conserved functions in actin dynamics across different cell types suggest that SHANK2 might influence the structure of hair bundles by regulating actin dynamics on the medial surface of developing HCs, which warrants further exploration.

## 4.2. RAP1 as an upstream regulator of SHANK2

Our study shows that the medial localization of SHANK2 is modulated by the small GTPase RAP1 (Figs. 26 and 28), which was identified as a binding partner of SHANK2 through screening of cDNA libraries from embryonic and neonatal inner ears (Table 1 and 2). RAP1 is known to regulate the localization of junctional proteins and is involved in forming cell-cell junctions [50,51]. In kidney epithelial cells, RAP1 regulates the localization of SHANK2 via the SPN-ANK domain, establishing tight junction and apico-basal polarity [40]. In our organ of Corti explants with RAP1 inhibitor or *Rap1a/b* double mutant mice results in the loss of SHANK2 localization on the medial apical surface of HCs and disrupts the unique bundle architecture, similar to the defects observed in *Shank2*-deficient mice (Figs. 25-26, 28, and 30). Importantly, neither the medial localization of aPKCζ and PARD6B nor the lateral localization of Gαi and GPSM2 are affected by RAP1 inhibition/mutation (Figs. 27-28), indicating that the role of RAP1 in protein recruitment in HCs is specific to SHANK2. Notably, RAP1 appears to play various roles in cochlear development beyond its regulation of SHANK2. In otic-specific *Rap1* cKO mice, we observed disorganization of the organ of Corti and degeneration of OHCs by 3 weeks, leading to severe hearing loss across all tested frequencies (Fig. 30). HC-specific *Rap1* mutants displayed reduced ABR wave I amplitudes at 6 kHz, while DPOAE thresholds remained unaffected at the same frequency (Fig. 31), suggesting potential impairments in auditory nerve function. These additional phenotypes may be linked to

RAP1's established roles in cytoskeletal dynamics—such as cofilin dephosphorylation [52,53]—and activity-dependent synaptic plasticity [54,55]. Further research is necessary to fully elucidate RAP1's contributions to cochlear patterning, hair cell integrity, and afferent signaling.

## 4.3. The role of the V-shaped OHC bundles from an evolutionary perspective

The V-shaped OHC hair bundle is a distinctive feature of the mammalian cochlea, unlike the straight or non-specific bundle patterns found in non-mammalian species [56]. In mammals, OHCs play a specialized role in amplifying sound within the cochlea, thereby improving hearing sensitivity and expanding the dynamic range [1,57]. Mammals are generally able to detect higher frequency sounds compared to other animals [58]. It has been hypothesized that the V-shaped configuration of the OHC bundle is optimized to minimize hydrodynamic drag, which is essential for OHC function, especially at high frequencies [59,60]. Computational models suggest that an optimal V-shape angle for minimizing flow resistance is around 100°, which matches the angles observed in the basal (high-frequency) region of the mouse cochlea [59,61]. However, assessing the functional relevance of hair bundle geometry has been challenging due to the absence of suitable animal models. Most mouse models with disrupted bundle morphology also present additional confounding phenotypes—such as hair cell misorientation, loss of the staircase architecture, cochlear shortening, or the presence of supernumerary hair cell rows—as observed in mutants of planar cell polarity (PCP) components, lateral polarity regulators, and ciliary proteins [4,5,8-15,62-64]. Other models, including *Bbs8* and *Alms1* mutants, display only mild and spatially restricted bundle disorganization affecting a small fraction of outer hair cells (~20%), and do not exhibit detectable auditory impairments [63,65]. In contrast, *Shank2* mutants, which specifically lack the U- or V-shaped architecture (Figs. 8-9), offer a unique opportunity to investigate the role of this architecture *in vivo*. At the onset of hearing (3 weeks), *Shank2* mutants show reduced auditory sensitivity only at high frequencies. Notably, this high-frequency hearing loss is closely linked to reduced OHC amplifier function rather than IHC-mediated auditory nerve activation (Fig. 10). These results support the hypothesis that the V-shaped architecture is crucial for processing high-frequency sound signals. Interestingly, in vestibular HCs, SHANK2 also localizes opposite the Gαi expression domain, but its absence does not affect the shape of the vestibular hair bundle (Figs. 4 and 6) or result in typical vestibular defects. Since the vestibular system is considered more ancient than the mammalian cochlea [66], it is possible that the

role of SHANK2 in forming V-shaped OHC bundles represents an evolutionary adaptation unique to the mammalian cochlea that enhances high-frequency hearing. A recent study on subterranean rodents, such as naked mole-rats, adds an intriguing dimension to this idea [67]. These animals, which hear in a much lower frequency range (125 Hz to 8 kHz) compared to mice or rats, exhibit OHCs with U-shaped bundles, similar to IHC bundles, rather than the typical V-shaped bundles [67]. While limited high-frequency hearing has been linked to impaired OHC function and other bundle abnormalities, including HC orientation and amino acid substitutions [67], these findings raise intriguing questions about the evolutionary adaptations of bundle architecture and its relationship to the frequency range of hearing.

## 4.4. Long-term protective role of U- or V-shaped Stereocilia

Our longitudinal study reveals that the distinctive bundle architecture is vital for maintaining hair bundle integrity and auditory function over time (Figs. 16-17). *Shank2* mutants show progressive hearing loss and degeneration of hair bundles, predominantly affecting mid-to-high frequencies (Figs. 16-17). While it is possible that SHANK2 might have additional roles in the mature cochlea, the reduced expression of Shank2 in postnatal hair cells (Fig. 1) and its minimal presence in mature hair cells (Fig. 12) [26] suggest that the early disruption of hair bundle architecture primarily drives the progressive decline in bundle integrity and hearing function. These findings indicate that the auditory hair bundle architecture not only enhances high-frequency hearing but also offers protection against age-related or other stress-dependent deterioration, especially in the high-frequency range. At 16 weeks, hearing loss in *Shank2* mutants is still closely associated to impaired OHC function, as evidenced by correlated shifts in ABR and DPOAE thresholds and decreased DPOAE amplitudes in the mid-to-high frequency range (Figs. 16 and 19). However, unlike at 3 weeks, there are significant reductions in ABR wave I amplitudes in 16-week-old systemic and HC-specific *Shank2* mutants, but not in SGN-specific mutants (Fig. 18). These results suggests that, in aged *Shank2* mutants, the impairment extends to IHC function activating auditory nerves. This long-term protective role for hair bundle integrity and auditory function may be particularly important considering that mammalian hair cells do not regenerate after injury.

### 4.5. The relationship between peripheral hearing loss and ASD

SHANK2 is a causative gene for autism spectrum disorder (ASD) and is involved in organizing multi-protein complexes at the postsynaptic density in the brain [36]. However, our study demonstrates that SGN-specific *Shank2* mutants do not exhibit significant structural or functional abnormalities (Figs. 13 and 15-19). These finding is consistent with the lack of auditory deficits in *Shank1* knockout mice [37], suggesting a functional redundancy among SHANK family proteins in SGNs or absence of function due to low expression levels. While there is no direct evidence linking SHANK2 mutations to hearing impairment in humans, some forms of ASD have been associated with hearing impairment, often exacerbating social difficulties due to impaired verbal communication [68-70]. Although sensory deficits in ASD have traditionally focused on central processing, recent studies have identified peripheral auditory deficits in ASD patients, including abnormal ABR and otoacoustic emissions [71-73]. Our results suggest a molecular connection between brain dysfunction and peripheral sensory deficits, highlighting the need for comprehensive and ongoing auditory evaluations in ASD patients, especially considering the progressive hearing loss observed in *Shank2* mutant mice.

## 5. Conclusion

We investigates the role of SHANK2 in establishing the distinctive U- or V-shaped hair bundles in developing cochlea. The medial localization of SHANK2 is regulated by the small GTPase RAP1. Furthermore, we also suggest that the significance of the unique hair bundle architecture for hearing function particulary at high-frequency as well as the long-term preservation of hair bundle integrity.

Our study provides new insights into the functional importance of the U- or V-shaped stereociliary bundle architecture in living organisms. These findings enhance our understanding of hair bundle development and its role in high-frequency hearing and long-term maintenance. Moreover, our research points to potential connections between hearing loss and ASDs, paving the way for future studies that explore the relationship between peripheral sensory deficits and neurodevelopmental disorders.

## References

1. Hudspeth AJ. Integrating the active process of hair cells with cochlear function. Nat Rev Neurosci 2014;15:600-14.
2. Gillespie PG, Muller U. Mechanotransduction by hair cells: models, molecules, and mechanisms. Cell 2009;139:33-44.
3. Furness DN, Richardson GP, Russell IJ. Stereociliary bundle morphology in organotypic cultures of the mouse cochlea. Hear Res 1989;38:95-109.
4. Ezan J, Lasvaux L, Gezer A, Novakovic A, May-Simera H, Belotti E, et al. Primary cilium migration depends on G-protein signalling control of subapical cytoskeleton. Nat Cell Biol 2013;15:1107-15.
5. Tarchini B, Jolicoeur C, Cayouette M. A molecular blueprint at the apical surface establishes planar asymmetry in cochlear hair cells. Dev Cell 2013;27:88-102.
6. Tarchini B, Lu X. New insights into regulation and function of planar polarity in the inner ear. Neurosci Lett 2019;709:134373.
7. Montcouquiol M, Kelley MW. Development and Patterning of the Cochlea: From Convergent Extension to Planar Polarity. Cold Spring Harb Perspect Med 2020;10.
8. Montcouquiol M, Rachel RA, Lanford PJ, Copeland NG, Jenkins NA, Kelley MW. Identification of Vangl2 and Scrb1 as planar polarity genes in mammals. Nature 2003;423:173-7.
9. Wang Y, Guo N, Nathans J. The role of Frizzled3 and Frizzled6 in neural tube closure and in the planar polarity of inner-ear sensory hair cells. J Neurosci 2006;26:2147-56.
10. Wang J, Mark S, Zhang X, Qian D, Yoo SJ, Radde-Gallwitz K, et al. Regulation of polarized extension and planar cell polarity in the cochlea by the vertebrate PCP pathway. Nat Genet 2005;37:980-5.
11. Siletti K, Tarchini B, Hudspeth AJ. Daple coordinates organ-wide and cell-intrinsic polarity to pattern inner-ear hair bundles. Proc Natl Acad Sci U S A 2017;114:E11170-E9.
12. Landin Malt A, Dailey Z, Holbrook-Rasmussen J, Zheng Y, Hogan A, Du Q, et al. Par3 is essential for the establishment of planar cell polarity of inner ear hair cells. Proc Natl Acad Sci U S A 2019;116:4999-5008.
13. Ozono Y, Tamura A, Nakayama S, Herawati E, Hanada Y, Ohata K, et al. Daple deficiency causes hearing loss in adult mice by inducing defects in cochlear stereocilia and apical

microtubules. Sci Rep 2021;11:20224.

14. Tarchini B, Tadenev AL, Devanney N, Cayouette M. A link between planar polarity and staircase-like bundle architecture in hair cells. Development 2016;143:3926-32.
15. Mauriac SA, Hien YE, Bird JE, Carvalho SD, Peyroutou R, Lee SC, et al. Defective Gpsm2/Galphai3 signalling disrupts stereocilia development and growth cone actin dynamics in Chudley-McCullough syndrome. Nat Commun 2017;8:14907.
16. Won H, Lee HR, Gee HY, Mah W, Kim JI, Lee J, et al. Autistic-like social behaviour in Shank2-mutant mice improved by restoring NMDA receptor function. Nature 2012;486:261-5.
17. Ha S, Lee D, Cho YS, Chung C, Yoo YE, Kim J, et al. Cerebellar Shank2 Regulates Excitatory Synapse Density, Motor Coordination, and Specific Repetitive and Anxiety-Like Behaviors. J Neurosci 2016;36:12129-43.
18. Yang H, Gan J, Xie X, Deng M, Feng L, Chen X, et al. Gfi1-Cre knock-in mouse line: A tool for inner ear hair cell-specific gene deletion. Genesis 2010;48:400-6.
19. Ghimire SR, Ratzan EM, Deans MR. A non-autonomous function of the core PCP protein VANGL2 directs peripheral axon turning in the developing cochlea. Development 2018;145.
20. Pan BX, Vautier F, Ito W, Bolshakov VY, Morozov A. Enhanced cortico-amygdala efficacy and suppressed fear in absence of Rap1. J Neurosci 2008;28:2089-98.
21. Urness LD, Wang X, Li C, Quadros RM, Harms DW, Gurumurthy CB, et al. Slc26a9(P2ACre) : a new CRE driver to regulate gene expression in the otic placode lineage and other FGFR2b-dependent epithelia. Development 2020;147.
22. Son EJ, Wu L, Yoon H, Kim S, Choi JY, Bok J. Developmental Gene Expression Profiling along the Tonotopic Axis of the Mouse Cochlea. PLoS One 2012;7:e40735.
23. Yoon H, Lee DJ, Kim MH, Bok J. Identification of genes concordantly expressed with Atoh1 during inner ear development. Anat Cell Biol 2011;44:69-78.
24. Petitpre C, Faure L, Uhl P, Fontanet P, Filova I, Pavlinkova G, et al. Single-cell RNA-sequencing analysis of the developing mouse inner ear identifies molecular logic of auditory neuron diversification. Nat Commun 2022;13:3878.
25. Shrestha BR, Chia C, Wu L, Kujawa SG, Liberman MC, Goodrich LV. Sensory Neuron Diversity in the Inner Ear Is Shaped by Activity. Cell 2018; doi:10.1016/j.cell.2018.07.007.

26. Li Y, Liu H, Giffen KP, Chen L, Beisel KW, He DZZ. Transcriptomes of cochlear inner and outer hair cells from adult mice. Sci Data 2018;5:180199.
27. Liu H, Chen L, Giffen KP, Stringham ST, Li Y, Judge PD, et al. Cell-Specific Transcriptome Analysis Shows That Adult Pillar and Deiters' Cells Express Genes Encoding Machinery for Specializations of Cochlear Hair Cells. Front Mol Neurosci 2018;11:356.
28. Orvis J, Gottfried B, Kancherla J, Adkins RS, Song Y, Dror AA, et al. gEAR: Gene Expression Analysis Resource portal for community-driven, multi-omic data exploration. Nat Methods 2021;18:843-4.
29. Moon H, Song J, Shin JO, Lee H, Kim HK, Eggenschwiller JT, et al. Intestinal cell kinase, a protein associated with endocrine-cerebro-osteodysplasia syndrome, is a key regulator of cilia length and Hedgehog signaling. Proc Natl Acad Sci U S A 2014;111:8541-6.
30. Jung ES, Park J, Gee HY, Jung J, Noh SH, Lee JS, et al. Shank2 mutant mice display a hypersecretory response to cholera toxin. J Physiol 2014;592:1809-21.
31. Han W, Shin JO, Ma JH, Min H, Jung J, Lee J, et al. Distinct roles of stereociliary links in the nonlinear sound processing and noise resistance of cochlear outer hair cells. Proc Natl Acad Sci U S A 2020;117:11109-17.
32. Bramhall NF. Use of the auditory brainstem response for assessment of cochlear synaptopathy in humans. J Acoust Soc Am 2021;150:4440.
33. Zhou X, Jen PH, Seburn KL, Frankel WN, Zheng QY. Auditory brainstem responses in 10 inbred strains of mice. Brain Res 2006;1091:16-26.
34. Schmeisser MJ, Ey E, Wegener S, Bockmann J, Stempel AV, Kuebler A, et al. Autistic-like behaviours and hyperactivity in mice lacking ProSAP1/Shank2. Nature 2012;486:256-60.
35. Jiang YH, Ehlers MD. Modeling autism by SHANK gene mutations in mice. Neuron 2013;78:8-27.
36. Monteiro P, Feng G. SHANK proteins: roles at the synapse and in autism spectrum disorder. Nat Rev Neurosci 2017;18:147-57.
37. Braude JP, Vijayakumar S, Baumgarner K, Laurine R, Jones TA, Jones SM, et al. Deletion of Shank1 has minimal effects on the molecular composition and function of glutamatergic afferent postsynapses in the mouse inner ear. Hear Res 2015;321:52-64.
38. Viberg A, Canlon B. The guide to plotting a cochleogram. Hear Res 2004;197:1-10.
39. Muller M, von Hunerbein K, Hoidis S, Smolders JW. A physiological place-frequency map

of the cochlea in the CBA/J mouse. Hear Res 2005;202:63-73.

40. Sasaki K, Kojitani N, Hirose H, Yoshihama Y, Suzuki H, Shimada M, et al. Shank2 Binds to aPKC and Controls Tight Junction Formation with Rap1 Signaling during Establishment of Epithelial Cell Polarity. Cell Rep 2020;31:107407.
41. Du TT, Dewey JB, Wagner EL, Cui R, Heo J, Park JJ, et al. LMO7 deficiency reveals the significance of the cuticular plate for hearing function. Nat Commun 2019;10:1117.
42. Etournay R, Lepelletier L, Boutet de Monvel J, Michel V, Cayet N, Leibovici M, et al. Cochlear outer hair cells undergo an apical circumference remodeling constrained by the hair bundle shape. Development 2010;137:1373-83.
43. Liu Y, Qi J, Chen X, Tang M, Chu C, Zhu W, et al. Critical role of spectrin in hearing development and deafness. Sci Adv 2019;5:eaav7803.
44. Sheng M, Kim E. The Shank family of scaffold proteins. J Cell Sci 2000;113 ( Pt 11):1851-6.
45. Salomaa SI, Miihkinen M, Kremneva E, Paatero I, Lilja J, Jacquemet G, et al. SHANK3 conformation regulates direct actin binding and crosstalk with Rap1 signaling. Curr Biol 2021;31:4956-70 e9.
46. Khwaja A, Sharpe CC, Noor M, Hendry BM. The role of geranylgeranylated proteins in human mesangial cell proliferation. Kidney Int 2006;70:1296-304.
47. Stefanini L, Lee RH, Paul DS, O'Shaughnessy EC, Ghalloussi D, Jones CI, et al. Functional redundancy between RAP1 isoforms in murine platelet production and function. Blood 2018;132:1951-62.
48. Durand CM, Perroy J, Loll F, Perrais D, Fagni L, Bourgeron T, et al. SHANK3 mutations identified in autism lead to modification of dendritic spine morphology via an actin-dependent mechanism. Mol Psychiatry 2012;17:71-84.
49. MacGillavry HD, Kerr JM, Kassner J, Frost NA, Blanpied TA. Shank-cortactin interactions control actin dynamics to maintain flexibility of neuronal spines and synapses. Eur J Neurosci 2016;43:179-93.
50. Knox AL, Brown NH. Rap1 GTPase regulation of adherens junction positioning and cell adhesion. Science 2002;295:1285-8.
51. Bonello TT, Perez-Vale KZ, Sumigray KD, Peifer M. Rap1 acts via multiple mechanisms to position Canoe and adherens junctions and mediate apical-basal polarity establishment.

Development 2018;145.

52. Lin KB, Freeman SA, Zabetian S, Brugger H, Weber M, Lei V, et al. The rap GTPases regulate B cell morphology, immune-synapse formation, and signaling by particulate B cell receptor ligands. Immunity 2008;28:75-87.
53. Wang JC, Lee JY, Christian S, Dang-Lawson M, Pritchard C, Freeman SA, et al. The Rap1-cofilin-1 pathway coordinates actin reorganization and MTOC polarization at the B cell immune synapse. J Cell Sci 2017;130:1094-109.
54. Kim YD, Park HG, Song S, Kim J, Lee BJ, Broadie K, et al. Presynaptic structural and functional plasticity are coupled by convergent Rap1 signaling. J Cell Biol 2024;223.
55. Xie Z, Huganir RL, Penzes P. Activity-dependent dendritic spine structural plasticity is regulated by small GTPase Rap1 and its target AF-6. Neuron 2005;48:605-18.
56. Tilney LG, Tilney MS, DeRosier DJ. Actin filaments, stereocilia, and hair cells: how cells count and measure. Annu Rev Cell Biol 1992;8:257-74.
57. Dallos P. Cochlear amplification, outer hair cells and prestin. Curr Opin Neurobiol 2008;18:370-6.
58. Heffner HE, Heffner RS. Hearing ranges of laboratory animals. J Am Assoc Lab Anim Sci 2007;46:20-2.
59. Ciganovic N, Wolde-Kidan A, Reichenbach T. Hair bundles of cochlear outer hair cells are shaped to minimize their fluid-dynamic resistance. Sci Rep 2017;7:3609.
60. Yarin YM, Lukashkin AN, Poznyakovskiy AA, Meissner H, Fleischer M, Baumgart J, et al. Tonotopic morphometry of the lamina reticularis of the guinea pig cochlea with associated microstructures and related mechanical implications. J Assoc Res Otolaryngol 2014;15:1-11.
61. Koo HY, Kim MA, Min H, Hwang JY, Prajapati-DiNubila M, Kim KS, et al. Follistatin regulates the specification of the apical cochlea responsible for low-frequency hearing in mammals. Proc Natl Acad Sci U S A 2023;120:e2213099120.
62. Jones C, Roper VC, Foucher I, Qian D, Banizs B, Petit C, et al. Ciliary proteins link basal body polarization to planar cell polarity regulation. Nat Genet 2008;40:69-77.
63. May-Simera HL, Petralia RS, Montcouquiol M, Wang YX, Szarama KB, Liu Y, et al. Ciliary proteins Bbs8 and Ift20 promote planar cell polarity in the cochlea. Development 2015;142:555-66.

64. Sipe CW, Lu X. Kif3a regulates planar polarization of auditory hair cells through both ciliary and non-ciliary mechanisms. Development 2011;138:3441-9.
65. Jagger D, Collin G, Kelly J, Towers E, Nevill G, Longo-Guess C, et al. Alstrom Syndrome protein ALMS1 localizes to basal bodies of cochlear hair cells and regulates cilium-dependent planar cell polarity. Hum Mol Genet 2011;20:466-81.
66. Gardner EP. The Senses: A Comprehensive Reference; 2010.
67. Pyott SJ, van Tuinen M, Screven LA, Schrode KM, Bai JP, Barone CM, et al. Functional, Morphological, and Evolutionary Characterization of Hearing in Subterranean, Eusocial African Mole-Rats. Curr Biol 2020;30:4329-41 e4.
68. Demopoulos C, Lewine JD. Audiometric Profiles in Autism Spectrum Disorders: Does Subclinical Hearing Loss Impact Communication? Autism Res 2016;9:107-20.
69. Beers AN, McBoyle M, Kakande E, Dar Santos RC, Kozak FK. Autism and peripheral hearing loss: a systematic review. Int J Pediatr Otorhinolaryngol 2014;78:96-101.
70. Chin RY, Moran T, Fenton JE. The otological manifestations associated with autistic spectrum disorders. Int J Pediatr Otorhinolaryngol 2013;77:629-34.
71. Bennetto L, Keith JM, Allen PD, Luebke AE. Children with autism spectrum disorder have reduced otoacoustic emissions at the 1 kHz mid-frequency region. Autism Res 2017;10:337-45.
72. Santos M, Marques C, Nobrega Pinto A, Fernandes R, Coutinho MB, Almeida ESC. Autism spectrum disorders and the amplitude of auditory brainstem response wave I. Autism Res 2017;10:1300-5.
73. Tas M, Yilmaz S, Bulut E, Polat Z, Tas A. Otoacoustic Emissions in Young Children with Autism. J Int Adv Otol 2017;13:327-32.

Abstract in Korean

# SHANK2가 부동섬모의 구조 형성과 청각 기능에 기여하는 역할 규명

포유류의 청각 기관은 효과적인 소리 전달을 위해 유모세포(hair cell) 표면의 부동섬모(Stereocilia) 다발의 정밀한 구조에 의존한다. 각 부동섬모 다발은 약 100개의 액틴(Actin)으로 채워진 부동섬모로 구성되어 있으며 3열 계단 패턴으로 배열되어 있고, 내유모세포(inner hair cell)에서는 넓은 U 자 모양을, 외유모세포(outer hair cell)에서는 V 자 모양을 형성하고 있다. 이 부동섬모 다발의 꼭지점은 달팽이관의 외측을 따라 일정하게 배열된다. 초기 발달 단계에서 고르게 분포되어 있던 미세융모(microvilli)들이 이렇게 독특한 부동섬모 다발 구조로 발달하는 것은 Gαi 와 GPSM2와 같이 외측(lateral) 표면에 있는 단백질들에 의해 제어되는 미세소관(microtubule) 기반 kinocilium 의 외측으로의 이동에 의해 조절된다. 이러한 외측 단백질들의 역할은 이미 연구가 잘 되어 있지만 내측에서 부동섬모의 형태를 결정하는 기전에 대해서는 아직 연구가 되어 있지 않다. 본 논문에서는 시냅스(synapse) 기능 및 자폐 스펙트럼 장애(autism spectrum disorder)와 관련된 단백질인 SHANK2가 유모세포의 내측(medial) 표면에서 U 자형 또는 V 자형 부동섬모 다발 구조를 형성하는데 중요한 역할을 한다는 것을 밝혔다. 유모세포 표면에서의 SHANK2 위치는 외측 표면 단백질인 Gαi 와 GPSM2나 내측 표면 단백질인 aPKCζ 와 PARD6B 와는 독립적으로 저분자량 GTP 가수분해효소(small GTPase) 중 하나인 RAP1에 의해 조절된다. *Shank2* 결손 마우스에서 달팽이관 유모세포는 전형적인 U 자형 또는 V 자형의 다발 구조를 잃고 단편화(fragmentation) 되거나 물결(Wavy) 형태의 다발을 가지는데 이때 kinocilium 의 위치와 계단식 패턴, 필수적인 부동섬모 간의 연결과 같은 다른 중요한 특성에는 영향을 주지 않는다. Tonotopic 축 전반에 걸친 광범위한 부동섬모 다발의 형태적 결함에도 불구하고 주로 고주파에서만 특이적으로 청력 손실이 관찰되며, 이는 외유모세포의 증폭 기능 손상에 의한 것으로 나타난다. 긴 시간에 걸친 추적 연구는 독특한 부동섬모 다발의 형태가 부동섬모 및 청각 기능의 장기적인 유지에 필수적임을 시사한다.

---

**핵심되는 말** : 유모세포, 부동섬모, 달팽이관, 청력 손실, 자폐 스펙트럼 장애